Multifaceted fusion defects converge on altered mitochondrial distribution and increased mutant mitofusin level in CMT2A models

Authors: **Olena O. Varuk [1], Amandine Ruiz [1], Célia Orengo[1], Amélie Cozzolino[1], Paul de Boissier [1], Aïcha Aouane[1], Thomas Rival [1, *]**

Affiliation: [1] Aix-Marseille Université, CNRS, IBDM, UMR 7288, F-13288 Marseille, France

Correspondence and materials: [*] thomas.rival@univ-amu.fr

Abstract

Charcot-Marie-Tooth type 2A neuropathy (CMT2A) is caused by a hundred different missense mutations in the mitofusin MFN2, a mitochondrial fusion factor. It is well established that different CMT2A alleles expressed in mitofusin deficient cells can exhibit varying levels of fusion activity. However, most CMT2A mutations are dominant. Therefore, to picture the complexity of CMT2A pathogenesis, it is crucial to define whether and how different fusion activity levels translate into different dominant properties. To explore the range of dominant properties among CMT2A alleles, we modelled in drosophila fourteen missense mutations reported in patients. We studied alleles from different mutation hotspots identified in MFN2 protein structure, alleles causing severe or mild forms of CMT2A, or alleles with different level of dominance in patients. Mitochondrial architecture analysis revealed a wide spectrum of composite dominant effects of variable expressivity. Fusion-inhibition and aggregation properties were found in mutants affecting catalytic motifs and hydrophobic cores, and exacerbation of mitochondrial fusion in mutants targeting domain interface. In these mutant categories, mitochondrial cytoplasmic distribution was disturbed to varying degrees that strongly correlate with neurotoxicity levels. Inhomogeneity of mitochondrial repartition was indeed associated with decreased endoplasmic reticulum-mitochondrion overlap, reduced mitochondrial content at neuromuscular junctions, higher locomotor deficits in flies and higher disease severity in patients. At the molecular scale, most CMT2A mutant proteins showed reduced ubiquitination and increased protein level, likely amplifying their dominant properties. Thus, CMT2A mutations induce a broad spectrum of fusion alterations converging towards altered mitochondrial distribution and mutant Mfn accumulation.

31 # Introduction

32 Mitochondria are connected and disconnected by fusion-fission cycles, a process supporting
33 mitochondrial homeostasis (Giacomello et al., 2020). Outer and inner mitochondrial
34 membranes (OMM, IMM) fusion is driven by mitofusin (Mfn) and OPA1 respectively
35 (Tilokani et al., 2018). The resulting content mixing optimises mitochondrial metabolism (Chen
36 et al., 2005), buffers mitochondrial damages (Ono et al., 2001) and supports mitochondrial
37 replication (Silva Ramos et al., 2019). Mitochondrial fission is driven by DRP1, facilitating
38 mitophagy (Twig et al., 2008) and mitochondrial transport (Verstreken et al., 2005). Neurons
39 being highly dependent on mitochondria, mitochondrial fusion-fission imbalance causes
40 neurological disorders (Bertholet et al., 2016). Mutations affecting human mitofusin 2 (MFN2)
41 cause type 2A Charcot-Marie-Tooth disease (CMT2A), a hereditary motor and sensory axonal
42 neuropathy (Stuppia et al., 2015). CMT2A is mostly due to dominant alleles leading to amino
43 acid (aa) substitutions, although rare recessive forms were described (Stuppia et al., 2015, Pipis
44 et al., 2020). Depending on the alleles, CMT2A can be early or late onset with severe to mild
45 symptoms (Stuppia et al., 2015, Pipis et al., 2020). Several evidence suggest that CMT2A
46 neuronal selectivity is due to low MFN1 expression in neurons (Kawalec et al., 2014). Indeed
47 MFN1, that is partially redundant with MFN2, is well known to rescue CMT2A mutations in
48 cell culture and *in vivo* (Detmer and Chan, 2007, Zhou et al., 2019, Shahin et al., 2023).

49 Mfns are large multi-domain proteins related to bacterial dynamin-like protein (BDLP) (Low
50 and Lowe, 2006, Low et al., 2009). A GTPase domain (GD) and two helix bundles (HB1, HB2)
51 are linked by hinges, and a short hydrophobic segment (TM) makes a OMM anchor. HB1 and
52 HB2 display two heptad repeats, HR1 and HR2, forming a coiled coil. Resolved structures of
53 truncated MFN1 and MFN2 (Koshiba et al., 2004, Cao et al., 2017, Yan et al., 2018, Li et al.,
54 2019), and *in silico* modelling of MFN2 (Beresewicz et al., 2018, Rocha et al., 2018) and yeast
55 Fzo1 (De Vecchis et al., 2019) provided insights into putative Mfns' activity. Interactions
56 through GD and HR2 might drive trans-oligomerisation and subsequent mitochondrial tethering
57 (Koshiba et al., 2004, Cao et al., 2017, Li et al., 2019). At hinges, GTP hydrolysis would then
58 drive an upward GD tilt (Yan et al., 2018, Li et al., 2019) and a scissor-like movement bringing
59 HB1 closer to HB2 (Beresewicz et al., 2018, Rocha et al., 2018, Brandner et al., 2019). This
60 open to a closed conformation switch would provide OMM fusion driving force (Formosa and
61 Ryan, 2016, De Vecchis et al., 2019). In this process, HR1-HR2 interaction might negatively
62 regulate fusion (Franco et al., 2016, Rocha et al., 2018), HR1 playing a role in lipid bilayer
63 destabilisation (Daste et al., 2018). Mfn activity is regulated by phosphorylation, oxidation and

ubiquitination (Giacomello et al., 2020). In yeast, Fzo1 oligomer disassembly is mediated by ubiquitination and subsequent proteasome-mediated degradation (Cohen et al., 2008, Alsayyah et al., 2020). In animals, several E3 ubiquitin ligases, including Parkin, ubiquitinate Mfns, in particular in mitophagy (Escobar-Henriques and Joaquim, 2019). Finally, in addition to mitochondrial fusion activity, Mfns establish contacts between mitochondria and various organelles (Gordaliza-Alaguero et al., 2019, Huo et al., 2022, Alsayyah et al., 2024).

Drosophila shares its mitochondrial fusion-fission machinery with mammals. Marf is the only ubiquitous Mfn (Hwa et al., 2002) whose neuronal depletion triggers mitochondrial fragmentation (El Fissi et al., 2018). Like mammalian Mfns, Marf is regulated by ubiquitination (Ziviani et al., 2010, Yun et al., 2014) and oxidation (Smith et al., 2019). Marf restores mitochondrial fusion in *Mfn1-Mfn2* knockout mouse cells, demonstrating the functional conservation between fly and mammalian Mfns (El Fissi et al., 2018). Marf appears closer to human MFN2 than MFN1 as the G2 motif isoleucine 108, causing MFN1's tenfold higher GTPase activity, is replaced by a threonine in MFN2 (T129) and Marf (T170) (Li et al., 2019). In addition, Marf depletion influences ER-mitochondrion interactions (Debattisti et al., 2014, Sandoval et al., 2014), a MFN2-specific function.

CMT2A mutations target residues in different MFN2 domains (Cartoni and Martinou, 2009) and might affect mitochondrial fusion in different ways. Consistently, several comparative studies revealed that different CMT2A alleles expressed in Mfn knockout cells can support varying levels of mitochondrial fusion (Detmer and Chan, 2007, Barsa et al., 2025, Joaquim et al., 2025). However, in the absence of endogenous MFN2, this did not tell whether and how these differences in terms of intrinsic activity translate into different dominant properties. To be in capacity to compare, among a large allelic series and in an *in vivo* context, potentially complex dominant properties, we chose drosophila as a model system. Flies present several advantages. The expression of a single mitofusin that approaches the situation in human neurons where MFN2 is preponderant. The accessibility of motor neurons that allows high resolution microscopy of mitochondria. Controlled transcription level and genetic background, and targeted expression in motor neurons. The possibility to correlate mitochondrial alterations with consequences at the organism scale, such as locomotor defects. Hence, we modelled and studied in flies fourteen CMT2A alleles, which represents the largest number of mutations ever compared so far, revealing an unanticipated broad spectrum of dominant effects.

Results

CMT2A mutations concentrated into structural hotspots

To highlight mutations hotspots in MFN2, we generated protein structure models based on BDLP closed and open conformations (Low and Lowe, 2006, Low et al., 2009), onto which we mapped CMT2A mutations (Figure 1A,B). From the literature, we listed ninety-four MFN2 residues mutated in CMT2A: 56% in GD, 22% in HB1, 11% in HB2, 7% in the hinges and 2% in TM (Figure 1A,B). Mutation frequency heat maps showed mutation enrichment in specific structural motifs (Figure 1C-E; Figure S1A). Secondary structures at the GD front were more affected than those at the back, particularly G1, G2, G3 and G4 catalytic motifs, and α1G, α2G, α3G and α4G helices (Figure 1C-E). Mutations affecting these regions may affect GTPase activity and oligomerisation as the homologous secondary structures form the dimer interfaces of MFN1 and BDLP (Figure S1B-E). The α3G C-terminal part and adjacent loop could form a GD-HB1 interface in MFN2 open conformation as observed in MFN1 and BDLP (Figure 1C; Figure S1B,D), whereas α2G and α3G would be at GD-HB2 interface in MFN2 closed conformation as for BDLP (Figure 1D; Figure S1E). Hence, mutations in these regions could affect the transition between open and closed conformations. In HB1 and HB2, CMT2A mutations concentrated in α3H1, α4H1 and α7H2 (Figure 1C,D) that are part of HR1 and HR2 involved in oligomerisation and fusion activity. Finally, the hinges that support Mfn conformational changes are largely affected (Figure 1C,D). Between GD and HB1, residues R94, R95, T356, K357 and S352 are mutated (Figure 1A). Homologous MFN1 residues are all involved in hinge 2 bending supporting GD movements upon GTP binding and hydrolysis (Figure S1B,C). CMT2A mutations also affected hinge 1 (Figure 1A,C,D), a region between HB1 and HB2 involved in open to closed conformational transition in BDLP (Figure S1D,E). Hence, CMT2A mutations target regions of functional importance and may lead to different molecular outcomes.

Modelling CMT2A allele diversity in flies

To compare CMT2A alleles from different hotspots, we mimicked them in drosophila. Marf and MFN2 share 45.5% of identical aa and 15.2% with similar properties (Figure S2A,B). When only considering CMT2A-related residues, identity and similarity reached 60.6% and 13.8% respectively (Figure S2A,B), reinforcing the idea that CMT2A-related residues are part of motifs critical for structure-function relationships. For our study in flies, we selected fourteen CMT2A aa substitutions, affecting conserved residues from different mutation hotspots:

129 R104W, H128R and R259L for G1, G2 and G4 ; D214N for α2G ; L248V and R250Q for α3G-
130 β5G ; R94W and K357N for hinge 2 ; L92P for α2H ; H361Y, R364W and R400P for HR1 ;
131 W740S and L745P for HR2 (Figure 1F). We included aa at the molecular surface, at the
132 interface between two domains, or buried within a domain (Figure 1F). In selecting these
133 residues, we checked that their localisation relative to protein domains and their lateral chain
134 orientation were conserved between Marf models and resolved structures of truncated MFN2
135 and MFN1 (Yan et al., 2018, Li et al., 2019). From there, a 'd' prefix refers to Marf residues
136 (Marf, MFN2, MFN1 correspondence: Figure S2C). As for human MFN2, dR104, dH128 and
137 dR259 localised in G1, G2 and G4 (Figure S3D; Figure S4A) and were at dimer interface, with
138 only dR259 forming hydrogen bonds as for its MFN1 counterpart (Figure S4B). Surface
139 orientation of dW740, that is part of HR2, was also conserved (Figure S3E; Figure S4C,E). In
140 contrast to their orientation in the GDP-bound state (Figure S4C), dR94, dR250, dK357 and
141 dR364 lateral chains were at the GD-HB1 interface in the GTP-bound state as for human Mfns
142 (Figure S3C; Figure S4D). Of note, Marf dD214 and dR364 and MFN2 D214 and R364
143 similarly faced HB2 in closed conformation models (Figure 1F; Figure S3B). GD residue dL248
144 and HB1 residues dL92, dH361 and dL745 associated with hydrophobic cores as for their
145 MFN2 equivalents (Figure S3E; Figure S4E,F). Finally, dR400 and R400 residues were
146 predicted at HB2 surface in both Marf and MFN2 models (Figure 1F; Figure S3F). In addition
147 to structural considerations, we explored differences in pathogenicity, by studying nine severe
148 early onset alleles (L92P, R94W, R104W, H128R, K357N, H361Y, R364W, R400P) and five
149 mild late onset alleles (D214N, R250Q, R259L, W740S, L745P) (Stuppia et al., 2015). Finally,
150 we include four alleles which implication is CMT2A was classified as "uncertain"
151 (https://www.ncbi.nlm.nih.gov/clinvar/) (D214N, R250Q, R400P, L745P), two of which being
152 proposed to be either recessive or semi-dominant mutations (D214N, R250Q) (Nicholson et al.,
153 2008, Piscosquito et al., 2015, Tomaselli et al., 2016). We introduced these fourteen aa
154 substitutions into the *Marf* coding sequence, inserted all CMT2A transgenes (*Marf* ^{CMT2A}) at the
155 same *locus* and expressed them in neurons using UAS/GAL4 system (Figure S5A). All *Marf*
156 constructs were tagged with HA. A control UAS *Marf* wild-type transgene (*Marf* ^{CTRL}) was
157 similarly generated providing an expression equivalent to 1.5 times that of endogenous Marf
158 (Figure S5B,C).
159

160 **CMT2A alleles form four phenotypic groups with composite features**

161 Using high-resolution confocal microscopy, we imaged for each CMT2A mutant the entire
162 mitochondrial network of motor neurons in living larval central nervous system (CNS). To

163 reveal mutant dominant properties, we analysed mitochondria in the presence of endogenous
164 Marf. The resulting phenotypes were complex and composite. Therefore, we scored three
165 categories of mitochondrial shape (fragmented, filamentous and enlarged) and two modes of
166 interaction (net-like and clustered). In parallel, we evaluated the fusion capacity of each mutant
167 in a *Marf* knockout background (*Marf* ^{KO}) by measuring mitochondrial tubule length. These
168 data were analysed by hierarchical clustering allowing us to classify our mutants into four
169 phenotypic groups and to evaluate their phenotypic distance from wild-type, *Marf*^{KO} and *Marf*
170 ^{CTRL} flies (Figure 2A). These mutant groups were named Grape, Tangle, Bulb and Peanut
171 according to their mitochondrial shape (Figure 2B).
172

173 **CMT2A mutants alter Mfn activity in different manners**

174 Consistent with a balanced fusion-fission equilibrium, wild-type motor neurons contained both
175 filamentous and fragmented mitochondria (Figure 2B, 3A; Figure S6A). Expression of *Marf*
176 ^{CTRL} transgene decreased mitochondrial fragmentation and triggered mitochondrial filament
177 fusion into net-like structures (Figure 2B, 3A; Figure S6A). On the opposite, *Marf*^{KO} triggered
178 a mitochondrial fragmentation rescued by *Marf* ^{CTRL} expression (Figure 2C; Figure 3B; Figure
179 S7A). In Grape mutants, including *dR94W*, *dR104W* and *dH128R*, motor neurons contained one
180 or two large and spherical clusters of fragmented mitochondria that often showed IMM swirls
181 or cristae loss (Figure 2B; Figure 3A; Figure S6B). Photoconversion experiments using
182 mit::dendra2 showed that, despite being packed, mitochondria were not connected (Figure
183 2D,E). Grape alleles did not restore tubules in *Marf* ^{KO} animals, showing fragmented and
184 clustered mitochondria (Figure 2C; Figure 3B; Figure S7B). Taken together, these data
185 demonstrate that Grape mutations are strong dominant negatives (DN) that do not affect Mfn
186 tethering but abolish wild-type Mfn fusion. Consistently, Grape mutants were the closest to
187 *Marf*^{KO} (Figure 2A). Within Tangle alleles *dL92P*, *dL248V*, *dR259L* and *dH361Y*, we observed
188 elongated clusters of packed mitochondrial tubules (Figure 2B; Figure 3A; Figure S6C) that did
189 not form an interconnected network (Figure 2D,E). In *Marf*^{KO} neurons, Tangle mitochondria
190 remained largely fragmented although few very short tubules were seen (Figure 2C; Figure 3B;
191 Figure S7C). Hierarchical clustering placed Tangle close to Grape and *Marf*^{KO} (Figure 2A). In
192 conclusion, Tangle mutants act as weak DN that cluster mitochondria without abolishing
193 endogenous Marf fusion activity. In Peanut mutants *dR250Q* and *dL745P*, mitochondria
194 essentially conserved their wild-type shape (Figure 2B; Figure 3A; Figure S6D). Because some
195 *dR250Q* neurons contained net-like mitochondria (Figure 3A), we quantified mitochondrial
196 length and branching to possibly detect subtle activity. This revealed that *dR250Q* and, to a

197 lesser extent, *dL745P* have a residual fusion capacity (Figure S8A-D). Consistently, *dR250Q*
198 formed mitochondrial tubules when expressed in *Marf*^{KO}, whereas *dL745P* only showed scarce
199 short elongated mitochondria (Figure 2C; Figure 3B; Figure S7D). According to their
200 phenotype, Peanut alleles segregated with wild-type, *dR250Q* being closer than *dL745P* (Figure
201 2A). Finally, Bulb mutants, including *dD214N*, *dK357N*, *dR364W* and *dW740S*, were placed by
202 hierarchical clustering close to *Marf* ^{CTRL} (Figure 2A). These alleles contained enlarged
203 mitochondria with normal cristae and no swelling (Figure 2B; Figure 3A; Figure S6E) and
204 restored mitochondrial tubules in *Marf*^{KO} (Figure 2C; Figure 3B; Figure S7E), showing that
205 Bulb alleles somehow favour fusion. Paradoxically, the hyperfused bulb-like mitochondria
206 were generally disconnected to the mitochondrial network, except for *dD214N* (Figure 2D,E).
207 Regarding structure-function relationship, there was no correlation between the mitochondrial
208 phenotype associated with a particular mutation and the specific protein domain affected by
209 that mutation (Figure 2A). However, most fusion-deficient alleles affected catalytic motifs and
210 hydrophobic cores whereas most of those that promote fusion affected interfaces between
211 domains (Figure 2A). Of note, the alleles that clustered closer to fusion-competent controls
212 (*dD214N*, *dR250Q* and *dL745P*) cause mild CMT2A symptoms in patients (Figure 2A). In
213 conclusion, CMT2A mutations have different consequences on Mfn activity in flies.
214

215 **Neurotoxicity level in CMT2A flies correlates with disease severity in CMT2A patients**

216 To determine whether the mutant mitochondrial phenotypes translate into neurotoxicity, we
217 analysed developmental lethality, photoreceptor neurodegeneration and locomotor
218 performance in flies upon neuron-specific expression of CMT2A mutations. Of note, startle-
219 induced locomotion was not dependent on vision (Figure S9). Consistent with their strong DN
220 activity, Grape mutants were the most severely affected. Only few escapers reached adulthood
221 exhibiting high photoreceptor loss and very poor locomotor ability (Figure 4A-C). Tangle and
222 Bulb phenotype expressivity varied between alleles with higher development lethality, stronger
223 neurodegeneration and lower locomotion in *dL248V, dL92P* and *dH361Y* for Tangle, and
224 *dR364W* and *dK357N* for Bulb (Figure 4A-C). Finally, Peanut mutants had no obvious toxicity
225 (except a weak degeneration in *dR250Q*) consistent with their mitochondrial phenotype (Figure
226 4A-C). Importantly for disease relevance, mutants with weak or no detectable neurotoxicity in
227 flies correspond to human alleles causing moderate CMT2A (*dR259L, dW740S* and *dL745P*)
228 or acting as semi-dominant (*dD214N*, *dR250Q*). In conclusion, whereas Grape and Peanut
229 phenotypes correlate with toxicity level, Tangle and Bulb alterations have variable outcomes.
230

231 **Neurotoxicity correlates with altered mitochondrial distribution**

232 Consistent with the above observations, only two mitochondrial traits significantly correlated
233 with decreased locomotor performance: the presence of clustered mitochondria and the loss of
234 tubular ones (Table S1). To understand the variable neurotoxicity level within our allelic series,
235 we searched for a common factor which strength could vary between alleles. One obvious
236 parameter was the distribution of mitochondria within motor neurons. Indeed, distribution could
237 be altered both by clustering in Grape and Tangle and by hyperfusion in Bulb. Quantification
238 revealed that mitochondria were homogeneously distributed in wild-type as well as in Peanut
239 mutants, whereas they had a focal localisation in Grape mutants (Figure 5A,B; Figure S10A).
240 Mitochondrial distribution inhomogeneity was intermediate for Tangle and Bulb alleles, and
241 varied between mutants (Figure 5A,B; Figure S10A). We then plotted for each allele
242 mitochondrial distribution index to locomotor performance and found a significant correlation
243 (Figure 5I). Hence, the more mitochondrial distribution was altered, the higher the
244 neurotoxicity. We then investigated whether altering mitochondrial distribution affects ER
245 organisation and interaction with mitochondria (Figure 5C; Figure S10B). Unlike mitochondria,
246 ER had a normal distribution in CMT2A neurons (Figure 5D). Hence, the asymmetric
247 distribution between ER and mitochondria led to decreased level of ER signal overlapping
248 mitochondria in the most toxic CMT2A alleles, including all Grape mutants, Tangle mutants
249 *dL248V, dL92P* and *dH361Y* and Bulb mutants *dR364W* and *dK357N* (Figure 5E). Grape
250 mitochondria were less associated to the ER that was abnormally fragmented within
251 mitochondrial clusters (Figure 5F; Figure S10B). In contrast, the overlap of mitochondria with
252 ER tubules was unchanged for Tangle and Bulb mutants and increased in Peanut mutants
253 (Figure 5F; Figure S10B). Because synaptic mitochondria are transported from neuronal soma,
254 we tested whether altered distribution in cell bodies could reduce mitochondria at
255 neuromuscular junctions (NMJ). Most CMT2A alleles had decreased mitochondrial content at
256 NMJ, the most severe depletion being observed for the most toxic mutants (Figure 5G,H; Figure
257 S10C). Statistical analysis revealed that reduced ER-mitochondrion overlap and NMJ
258 mitochondria correlated with inhomogeneous mitochondrial distribution and locomotor deficit
259 (Table S1). In conclusion, the extent to which a CMT2A allele is toxic in flies is proportional
260 to the extent of which it alters mitochondrial distribution.

261

262 **Grape and Tangle alleles are insensitive to Parkin overexpression**

263 Searching for mechanisms that could commonly rescue Grape, Tangle and Bulb mutants, we
264 thought that increasing Mfn turnover could help neurons to cope with defective CMT2A

265 proteins. In flies, Marf is targeted to degradation by E3 ubiquitin ligase Parkin (Ziviani et al.,
266 2010). Consistently, Parkin overexpression (*parkin*^{OE}) in *Marf* ^{CTRL} increased fragmentation and
267 reduced fusion into net-like structures (Figure 6A,B), whereas *parkin* knockdown induced
268 enlarged bulb-like mitochondria (Figure S11A). In Grape and Tangle mutants, *parkin*^{OE} did not
269 prevent mitochondrial clustering suggesting that the mutant proteins were resistant to Parkin-
270 dependent degradation (Figure 6A,B; Figure S11B,C). In Tangle, *parkin*^{OE} triggered a
271 fragmentation of mitochondria that was stronger than the one observed in *Marf* ^{CTRL} control
272 (Figure 6A,B; Figure S11C). This confirmed that Tangle alleles are inactive and suggested that
273 the mitochondrial tubules found in these mutants were generated by endogenous Marf.
274 Similarly, *parkin*^{OE} led to mitochondrial fragmentation in Peanut mutants (Figure 6A,B; Figure
275 S11D). *Parkin*^{OE} induced mitochondrial clustering in *dR250Q* (Figure 6A,B; Figure S11D),
276 possibly reflecting a cryptic DN property revealed by wild-type Marf degradation. Consistent
277 with these mitochondrial phenotypes, *parkin*^{OE} increased developmental lethality in Grape,
278 Tangle and Peanut mutants supporting the idea that Parkin might target wild-type but not mutant
279 Marf (Figure 6C). In contrast, *parkin*^{OE} lowered the occurrence of enlarged mitochondria in
280 Bulb mutants (Figure 6A,B; Figure S11E), and developmental lethality was not exacerbated by
281 Parkin except for *dK357N* (Figure 6C). Taken together, these observations demonstrated that
282 most CMT2A fly mutants are insensitive to Parkin.
283

284 **Reduced ubiquitination and increased protein levels in CMT2A mutant flies**

285 We then investigated whether CMT2A mutations interfere with Marf ubiquitination. Our *Marf*
286 ^{CTRL} and *Marf* ^{CMT2A} transgenes being HA-tagged, we could specifically analysed these
287 recombinant proteins independently of endogenous Marf. We first determined Marf
288 ubiquitination profile in *Marf* ^{CTRL} flies. Anti-HA western blot against immuno-precipitated
289 Marf revealed three main bands at 100 kDa, 110 kDa and 130 kDa (Figure 7A). Anti-Ubiquitin
290 staining demonstrated that the 100 kDa band corresponded to native Marf whereas the 110 and
291 130 kDa bands were ubiquitinated forms (Figure 7A). Of note, a minor band with higher
292 molecular weight and higher ubiquitination was also detected. Parkin was involved in the
293 formation of the two main Marf ubiquitinated forms as they both decreased upon *parkin*
294 knockdown (*parkin*^{KD}) (Figure 7B). We next determined ubiquitinated *versus* native Marf ratios
295 in CMT2A mutants. Ubiquitination was reduced for all CMT2A proteins except for *dD214N*
296 (Figure 7C,D). Interestingly, the ubiquitination level of mutant proteins correlated with the
297 fusion capacity measured in *Marf* ^{KO} CMT2A flies (Table S1). This ubiquitination defect was
298 followed by increased mutant Marf level for most CMT2A strains (Figure 7E) which

299 significantly correlated with decreased locomotor performance as well as focal distribution and
300 clustering of mitochondria (Table S1). In conclusion, CMT2A mutations affect Marf
301 ubiquitination, likely potentiating their dominant properties through mutant protein
302 accumulation.
303

304 Discussion

305 We showed that CMT2A mutations are enriched in specific MFN2 regions, many of which
306 previously shown to play key roles in Mfns and BDLP activity. These hotspots include GTP
307 binding pocket motifs and GD secondary structures that form the dimer interface. In HB1,
308 mutations accumulates in HR1 and HR2 which regulate trans-oligomerisation and membrane
309 fusion. CMT2A mutations also strongly affect the flexible hinges supporting GD movements
310 and HB1-HB2 closure. Finally, it is noticeable that several residues localize at the interface
311 between GD and HB1 in the open conformation. Our observations have several general
312 implications. For clinicians, the hotspots we defined could improve MFN2 mutation scoring: a
313 novel variant having more chance to be pathogenic if it targets an aa from a hotspot. CMT2A
314 hotspots could also orient structure-function studies as they highlight specific structures of
315 interest and specific residues within these structures which analysis could improve our
316 knowledge on Mfn molecular mechanism.
317

318 We classified our CMT2A mutants into four groups: Grape, Tangle, Peanut and Bulb. Grape
319 mutants act as strong DN with a high aggregative property, observed even in the absence of
320 endogenous Marf. Hence, oligomerisation capacity was retained but fusion capacity was lost.
321 Such phenomenon could occur because catalytic pocket mutants *dH128R* and *dR104W* would
322 affect GTP hydrolysis, or because hinge 2 mutant *dR94W* would compromise conformational
323 changes triggered by GTP hydrolysis. The fact that *dL248V* had a similar, although milder,
324 Grape phenotype could result from the alteration of GD hydrophobic core in which L248 is
325 implicated. In *Marf* ^{KO}, Tangle alleles had fragmented mitochondria that did not cluster. In
326 contrast, they induced mitochondrial aggregation in the presence of wild-type Marf. However,
327 unlike Grape mutants, Tangle alleles did not fully counteract wild-type Marf activity,
328 mitochondria remaining tubular. This suggests that Tangle mutant proteins do not efficiently
329 assemble with each other to form fusion complexes, but can interact with wild-type Marf. In
330 that case, the resulting fusion complexes might remain locked at the docking step, causing
331 mitochondrial clustering. Two Tangle mutants, *dL92P* and *dH361Y*, are part of a large

332 hydrophobic network maintaining HB1 helices (Yan et al., 2018, Li et al., 2019), another one,
333 *dR259L*, is part of G4 catalytic motif, and a third one, *dR400P*, is a HB2 surface residue.
334 Interestingly, R259 in addition of being part of the catalytic pocket, as for R104 and H128, is
335 involved in MFN2 dimerisation through an interaction with E230 from the opposite molecule
336 (Yan et al., 2018, Li et al., 2019). Hence, *dR259L* by reducing the ability of mutant molecules
337 to interfere with wild-type ones could lead to a weaker DN phenotype than *dR104W* and
338 *dH128R*. Peanut mutants had reduced fusion activity, *dR250Q*, at the GD-HB1 interface, being
339 more active than *dL745P* that is part of HB1 hydrophobic core (Li et al., 2019). In $Marf^{KO}$ flies,
340 Bulb mutants led to mitochondrial tubule formation and, in wild types, they formed enlarged
341 bulb-shape mitochondria typically described in mammalian and fly cells deficient for DRP1 or
342 overexpressing Mfn (Wakabayashi et al., 2009, Rival et al., 2011, Kageyama et al., 2012, El
343 Fissi et al., 2018). Of note, these hypertrophied mitochondria were generally disconnected from
344 the rest of the network likely interfering with global mitochondrial content mixing. In Detmer
345 and Chan's landmark study, four out of nine CMT2A mutations restored mitochondrial tubules
346 in *Mfn1-Mfn2* double knockout cells (Detmer and Chan, 2007). Later, some CMT2A alleles
347 were associated with excessive fusion in patient fibroblasts (Chevrollier et al., 2012, Codron et
348 al., 2016), HeLa cells (Das et al., 2022a, Das et al., 2022b, Das et al., 2024) and fly models (El
349 Fissi et al., 2018). Consistent with our drosophila data, human $MFN2^{D214N}$ and $MFN2^{W740S}$ were
350 reported as fusion competent (Detmer and Chan, 2007, Li et al., 2019) whereas human
351 $MFN2^{K357T}$ and $MFN2^{R364W}$ were associated with enlarged mitochondria in mouse and human
352 cells respectively (Stavropoulos et al., 2021, Das et al., 2022a, Das et al., 2024). The mechanism
353 by which Bulb mutants lead to increased mitochondrial size is unknown and may differ between
354 alleles as they target different protein regions: HB1-HB2 interface for *dD214N*, GD-HB1 and
355 HB1-HB2 interfaces for *dR364W*, hinge 2 for *K357N* and HR2 surface for *W740S*. Recent
356 studies suggested that complex mechanisms could be involved, the hyperfusion caused by
357 $MFN2^{R364W}$ in human cells being related to an inhibition of mitochondrial fission consecutive
358 to the imbalance between MFN2 and DRP1 ubiquitination (Das et al., 2022a, Das et al., 2022b).
359

360 Mfns from yeast, flies and mammals are targets of E3 Ubiquitin ligases regulating Mfn steady
361 state level and functions, in particular mitophagy (Escobar-Henriques and Joaquim, 2019,
362 Alsayyah et al., 2020). In drosophila, Parkin ubiquitinates Marf and negatively regulates its
363 expression level (Ziviani et al., 2010). When overexpressed in CMT2A flies, Parkin attenuated
364 Bulb phenotype but did not counteract mitochondrial clustering in Grape and Tangle. In Tangle
365 mutants, mitochondria became more fragmented showing that wild-type Marf molecules were

366 efficiently targeted by Parkin. Regarding Peanut group, Parkin induced mitochondrial
367 clustering in *dR250Q*. This suggests that degrading wild-type Marf has revealed a cryptic
368 aggregative property, an observation consistent with the semi-dominance described in R250Q
369 patients (Tomaselli et al., 2016). The fact that Parkin is active on Bulb mutants that restores
370 mitochondrial tubules formation in $Marf^{KO}$ flies, but not on Grape, Tangle and Peanut alleles
371 that are fusion-defective, suggests a relationship between Marf activity and Parkin-mediated
372 ubiquitination. Interestingly, Fzo1 ubiquitination and subsequent proteasome-dependent
373 degradation are required for mitochondrial fusion in yeast. GD mutations, including a CMT2A-
374 related one, abolish Fzo1 ubiquitination and degradation by impairing Fzo1 interaction with
375 SCF^{Mdm30} ubiquitin ligase (Amiott et al., 2009, Anton et al., 2011, Cohen et al., 2011). Indeed,
376 altered GTPase activity would prevent a conformational change required to reveal an otherwise
377 hidden SCF^{Mdm30} binding site (Cohen et al., 2011). Interestingly, *mdm30* inactivation trigger
378 Fzo1 accumulation, paradoxically associated with mitochondrial fragmentation and
379 aggregation (Cohen et al., 2011). Because promoting Fzo1 degradation independently of
380 SCF^{Mdm30} rescues this phenotype, it was proposed that Fzo1 turnover positively regulates
381 mitochondrial fusion (Cohen et al., 2011). A similar mechanism could contribute to
382 mitochondrial clustering in Grape and Tangle mutants. Consistently, when we looked at the
383 ubiquitination status of mutant Marf by western blot, we found that ubiquitination was reduced
384 in all loss-of-function mutants (*dR104W*, *dH128R*, *dL92P*, *dR94W*, *dL248V*, *dH361Y*, *dL745P*).
385 Although the overall decrease was lower, we also found reduced ubiquitination in the mutants
386 that restored mitochondrial tubulation in $Marf^{KO}$ (*dR250Q*, *dK357N*, *dR364W* and *dW740S* but
387 not *dD214N*). This suggests that *dR250Q*, *dK357N*, *dR364W* and *dW740S* mutations somehow
388 perturb the functional relationship between Marf and Parkin when Parkin is expressed at steady
389 state level, this alteration being however compensated by Parkin overexpression. Consistent
390 with a role of ubiquitination in Marf turnover, we observed increased expression level for most
391 CMT2A proteins. This observation suggests that defective ubiquitination increases mutant to
392 wild-type protein ratio, possibly contributing to CMT2A alleles dominant properties. However,
393 although the most neurotoxic alleles were the most overexpressed (*dR104W*, *dH128R*, *dL92P*),
394 phenotype severity did not correlate with expression levels for the all mutants. This
395 demonstrates that the allele toxicity is primarily determined by its impact on Mfn activity, the
396 increased expression level acting as an amplifier.
397
398 We observed varying degrees of neurotoxicity in our allelic series. Consistent with their
399 phenotypes, Grape alleles showed the highest toxicity in flies and Peanut the lowest. Tangle

400 and Bulb mutants had intermediate toxicity which degree varied depending on the allele.
401 Overall, we found that reduced locomotor performance correlated to the extent to which
402 mitochondria had a focal distribution in neuronal cytoplasm. The improper mitochondrial
403 repartition could be due to aggregation or unbalanced fusion depending on mutant group. This
404 mitochondrial sequestration would presumably create dysfunctional cytoplasmic regions by
405 affecting the delivery of mitochondria to the areas where their activity is needed, in particular
406 synapses, and by impairing the functional wiring of mitochondria to the rest of the organelle
407 community. In addition, the abnormal Grape, Tangle and Bulb mitochondria were poorly
408 connected to the network, possibly exacerbating the effects of their inefficient distribution.
409 Importantly, phenotype severity in flies correlated well with disease severity in human. Grape
410 mutants (*dR94W*, *dR104W*, *dH128R*, *dL248V*) as well as Tangle and Bulb mutants (*dL92P*,
411 *dH361Y*, *dR364W*, *dK357N*) with the lower locomotion in flies corresponds to MFN2 mutations
412 causing severe and early onset CMT2A (Kijima et al., 2005, Calvo et al., 2009, Stuppia et al.,
413 2015). Conversely, the less affected Tangle (*dR259L*) and Bulb (*dD214N*, *dW740S*) mutants as
414 well as Peanut mutants (*dR250Q*, *dL745P*) correspond to MFN2 mutations associated with mild
415 and late onset CMT2A (Nicholson et al., 2008, Ajroud-Driss et al., 2009, Nakhro, 2013, Stuppia
416 et al., 2015). Our data support the pathogenicity of four human alleles whose involvement in
417 CMT2A was classified as uncertain (D214N, R250Q, R400P, and L745P), as the related
418 mutations in flies affect MARF activity. Regarding L745P, the fly-related mutation causes a
419 loss of function without dominant properties. This suggests a sensitizing condition that might
420 trigger haploinsufficiency in patients. Finally, the phenotypes of *dR250Q* and *dD214N* flies
421 very well echo the clinical data. Indeed, the R250Q and D214N alleles only trigger CMT2A
422 when patients are compound heterozygous and were proposed to act as semi-dominant
423 (Nicholson et al., 2008, Piscosquito et al., 2015, Tomaselli et al., 2016).
424
425 Taken together, our findings support the use of drosophila as a test tube to validate the
426 implication of novel MFN2 genetic variants in CMT2A and predict their putative severity.
427 Overall, these data show a strong correlation between phenotype strength in flies and disease
428 severity in humans, supporting the relevance of drosophila in the study of CMT2A disease.
429
430
431
432

433 # Methods

434

435 **Protein sequence analysis and structure modelling**

436 BLAST was used to retrieve the sequences of Mfns (Marf: 11 insect species ; MFN1 and MFN2:
437 11 vertebrate species) and of BDLPs (26 *Nostoc* species). BDLPs were aligned using T-Coffee
438 (Notredame et al., 2000) simple alignment tool based on ClustalW algorithm. Mfns were
439 aligned using the PSI-Coffee (Notredame et al., 2000). Aa identity and similarity were
440 calculated with SMS Ident and Sim (https://www.bioinformatics.org/sms2/ident_sim.html)
441 using default parameters (GAVLI, FYW, CM, ST, KRH, DENQ, P). Outputs of these two
442 alignments were merged using the T-Coffee Combine alignment algorithm. MFN1, MFN2,
443 Marf and BDLP linear alignment was manually refined according to the structural alignment
444 of MFN2 (PDB: 6JFK) and BDLP (PDB: 2J68) (Low and Lowe, 2006, Li et al., 2019) obtained
445 using ChimeraX (Goddard et al., 2018). This alignment was used for template-based molecular
446 modelling of MFN2 and Marf using BDLP structures in open and closed conformations (PDB:
447 2J68, 2W6D) (Low and Lowe, 2006, Low et al., 2009). As MFN2 and Marf have longer N-
448 terminal tails than BLDP, we built N-terminal truncated models: MFN2-Δ1-23 and Marf-Δ1-
449 60, respectively. Transmembrane regions were predicted with TMpred (Cuthbertson et al.,
450 2005). A single-template modelling script was used to generate over 100 of closed- and open-
451 conformation models using the MODELLER program (v 10.0) (Sali and Blundell, 1993). The
452 GDP ligand was docked to the catalytic pocket either by modelling procedure, or using
453 ChimeraX structure analysis tool (https://www.cgl.ucsf.edu/chimerax/). In the end, one
454 homology model was selected based on the lowest *modpdb* value for the closed and open
455 conformations of MFN2 and Marf. The hydrogen were then added on a MolProbity (Chen et
456 al., 2010). The stereochemical quality was assessed using MolProbity and ProCheck. Z-score
457 and local energy quality were determined using ProSA (Wiederstein and Sippl, 2007). Models
458 of Marf dimers were generated using machine learning-based modelling (Jumper et al., 2021)
459 with AlphaFold3 algorithm (https://alphafoldserver.com/). The resulting model was in a GDP-
460 bound-like state (GD tilted upward) as found in resolved GDP-bound MFN2 and MFN1
461 truncated structures (Yan et al., 2018, Li et al., 2019). Marf with GTP-bound-like state (GD
462 tilted downward) was generated with AlphaFold2, providing truncated MFN1 GTP-bound
463 structure (PDB: 5YEW) as a template and reducing multiple alignment size (*max_msa*) (setting:
464 16:32)

465 (https://colab.research.google.com/github/sokrypton/ColabFold/blob/main/AlphaFold2.ipyn).
466 Graphical representation and residue mapping were generated using ChimeraX.

467

468 ***Drosophila* stocks and culture**

469 *Marf UAS* lines: *Marf* coding sequence was amplified from w^{1118} fly cDNAs and inserted into
470 the pUASt-derived vector pPHW (from T. Murphy) by Gateway cloning using pDonr221 as
471 intermediate. This *Marf* sequence differed from the one on Flybase by silent mutations (natural
472 polymorphisms and a synthetic EcoNI site introduced for screening convenience)
473 (Supplementary sequence). *Marf* 5' and 3' UTRs were not included. A CACC kozak sequence
474 (Acevedo et al., 2018) and three N-terminal HA tags were added. All CMT2A mutations were
475 made by PCR (CloneAmp HIFI, Takara Bio). Constructs were verified by Sanger sequencing.
476 Vectors carrying *Marf* wild-type or mutant alleles were inserted into chromosome 2L (25C6)
477 by phiC31-mediated transgenesis using *w* ; *attP40* flies (Bestgene). Strains from BDSC: *elav-*
478 *GAL4* (#458), *OK371-GAL4* (#26160), *UAS-myr::mRFP* (#7119), *UAS-KDEL::GFP* (#9898),
479 *UAS-parkin_IR* (#38333, TRiP.HMS01800) and Y *3xP3-DsRed2* (#41459). The following
480 lines were previously described by the authors: *UAS-mit::dendra2*, *Marf KO* (El Fissi et al.,
481 2018) and *UAS-mit::mKate2* (Poliacikova et al., 2023). *UAS-Parkin* was a generous gift from
482 Ming Guo. GAL4/UAS fly crosses were grown at 29°C on a cornmeal-agar diet. We used third
483 instar wandering larvae, except for $Marf^{KO}$ larvae which stage could not be precisely
484 determined as Mfn loss of function alters larval developmental (Sandoval et al., 2014, El Fissi
485 et al., 2018).

486

487 **Adult fly emergence quantification**

488 *elav-GAL4 / Y ; UAS-mit::dendra2* males were crossed to $UAS\text{-}Marf^{CMT2A\ or\ WT}$ females
489 providing a progeny in which females but not males expressed CMT2A alleles as *elav-GAL4* is
490 inserted on the X chromosome. Developmental lethality was assessed by counting the number
491 of females and males in the adult offspring. Similar approach was applied to crosses made using
492 *OK371-GAL4/CyO* flies as only the wild-type wing progeny express GAL4.

493

494 **Analysis of photoreceptor degeneration**

495 $elav\text{-}GAL4\ ;\ UAS\text{-}Marf^{CMT2A\ or\ WT}\ /\ UAS\text{-}mit::dendra2$ female flies were anesthetised with CO_2
496 and decapitated with a micro-scissor. The back of the head was immediately glued with methyl
497 cyanoacrylate onto a glass slide and the eyes covered with immersion oil (Leica Type F).

498 Observations were made on a Zeiss Axioplan 2 microscope at 63X with light at maximum
499 intensity and diaphragm at lower aperture. Photoreceptor degeneration was scored by counting
500 the number of ommatidia with less than seven rhabdomeres. We analysed on average 175
501 ommatidia from 8 individuals per condition. Statistical analysis was performed using Mann-
502 Whitney U test.
503
504 **Locomotor assay**
505 Fly development was carried out at 29°C, except for *dR94W*, *dR104W*, and *dH128R* that were
506 grown at 25°C to reduce developmental lethality and get adults. Adult flies (*elav-GAL4 ; UAS-*
507 *Marf*$^{CMT2A\ or\ WT}$ */ UAS-mit::dendra2*) were aged 10 days by group of 15 flies, the culture vials
508 being changed every two days. Locomotor performance was determined by startle-induced
509 negative geotaxis (SING). We used an empty culture vial in which one piece of PU foam plug
510 was inserted at the bottom and one at the top defining a free space of 65 mm height. A dozen
511 of flies were introduced in the vial, allowed to recover from CO_2 anaesthesia (30 min) and
512 tapped down to the bottom to trigger SING. A picture of the tube was taken 5 sec later using a
513 digital camera. The height reached by each flies was measured using ImageJ. To test for the
514 effect of vision on SING, a group of flies was first assessed into the complete darkness and then
515 in the light. Three to four independent races involving a total of 20-30 flies were performed per
516 condition. Statistical analysis was performed using Mann-Whitney U test.
517
518 **Live confocal imaging**
519 Third instar larvae tissues were very rapidly dissected, mounted and observed under the
520 microscope (<5 min). *Marf*^{KO} males were sorted thanks to a *3xP3-mCherry* Y chromosome.
521 CNS or ventral cuticle were mounted in PBS. Two bands of double-face tape were placed on
522 both side of the samples to avoid crushing between the coverslips and the slide. We imaged
523 dorsal motor neuron clusters of the ventral nerve cords and NMJs located at the surface of
524 muscles attached to the ventral cuticle. Z-image stacks (interval 0.2 µm) covering the whole
525 depth of motor neuron clusters or NMJs were acquired under a Zeiss LSM880 confocal
526 microscope at low laser intensity (<10%) with 63X (NMJs) or 100X (cell bodies) objectives.
527 For high resolution observations, we used a Airyscan detector.
528
529 **Mitochondrial morphology analysis**
530 Airyscan-acquired Z-image stacks of living motor neurons (dorsal clusters of larval ventral
531 nerve cord) expressing mit::dendra2 were submitted to deconvolution (Zen 2.3SP1 software

532 with auto-settings). To analyse mitochondria in a wild-type background, we used Z-stacks, Z-
533 projection (Fiji, Temporal Colour Coder) and 3D reconstruction (Fiji, 3D project) as templates
534 for scoring in blind pre-defined morphological mitochondrial traits i.e. fragmented,
535 filamentous, enlarged, net-like and clustered. To analyse mitochondria in Peanut and in *Marf*
536 ^{KO} flies, mitochondria were automatically segmented on confocal Z-projections of 10 images
537 using a Weka classifier (Fiji, https://imagej.net/plugins/tws/). Then, total branch length and
538 number were determined using MitoAnalyser (Fiji,
539 https://github.com/AhsenChaudhry/Mitochondria-Analyzer) with default parameters.
540

541 **Hierarchical clustering**

542 First, we submitted to hierarchical clustering the quantifications of mitochondrial shape
543 obtained when CMT2A mutations were expressed in a wild-type background. In these
544 quantifications, the presence of 5 mitochondrial traits was scored in each cell analysed (see
545 above). Using the R package *stats* version 4.1.3, the distance matrix between each cell was
546 calculated using the *dist* function with the *binary* method (as data were represented by the
547 absence or presence of a mitochondrial trait). Then, a mean distance was calculated between
548 each mutation. Then, the distance matrix between each mutation in a *Marf*^{KO} background was
549 calculated for the mean mitochondrial length, for the percentage of fragmented mitochondria
550 (length below 0.6 µm) and for the percentage of filamentous mitochondria (length above 1.4
551 µm) using the *dist* function with the *euclidean* method. Then, a hierarchical clustering between
552 this new matrix and the previous matrix of mean distance of the presence/absence of the five
553 mitochondrial traits was calculated using *hclustcompro* with the method *ward.D* from the R
554 package *SPARTAAS* version 1.2.4 (https://CRAN.R-project.org/package=SPARTAAS), which
555 is a tool allowing to combine distance matrices from two different sources to create this
556 clustering and defined potential clusters. We let the tool calculates the α parameter, which is
557 the mixing parameter giving different weights to each matrix (here α=0.59, giving more weight
558 to the wild-type background matrix). Finally, the dendrogram created was also converted to
559 newick format using the package *ape* version 5.7-1 (Paradis and Schliep, 2019) and visualised
560 using SeaView version 5.0.5 (Gouy et al., 2021).
561

562 **Electron Microscopy**

563 Larval CNS were rapidly dissected, placed on a glass slide, incubated in a drop of fixation
564 solution (FS) (2% paraformaldehyde, 2.5% glutaraldehyde, 5mM $CaCl_2$, 0.1mM Na

565 cacodylate) for 30 min at room temperature and embedded in a drop of 2% low melting agarose.
566 Agarose cubes containing larval CNS were cut out with a scalpel and placed in FS for 24 hr at
567 4°C. This was followed by 2 hr post-fixation (2.5% glutaraldehyde, 0.8% osmium tetroxide,
568 0.1mM Na cacodylate) at 4°C. Ultrathin Epon plastic sections were contrasted in 2% uranyl
569 acetate for 10 min and lead citrate for 2.5 min and observed with a Tecnai G2 TEM at 200 kV.
570

571 **Mitochondrial content mixing**

572 Dissected CNS from *OK371-GAL4, 2 X [UAS-mit::dendra2] /UAS-HA::Marf* larvae were
573 observed under a Ropper-Nikon spinning disc confocal microscope equipped with photo-
574 conversion module controlled by Metamorph. Mit::dendra2 was photoconverted at 450nm with
575 5% laser power for 1800 ms (300 iterations). Green (excitation 488nm) and red (excitation
576 545nm) mit::dendra2 signals were acquired repetitively during a time window of 180 sec. The
577 photoconverted areas of the first image (area Ai) and last image (area Af) were measured using
578 Fiji to calculate a diffusion index Af/Ai expressed as percent of control.
579

580 **Mitochondrial and ER distribution**

581 Confocal images of *OK371-GAL4, UAS-mit::dendra2/UAS-HA::Marf ; UAS-myr::mRFP* third
582 instar larvae were cropped around individual motor neurons according the myr::mRFP signal
583 and the size of all images adjusted to 128x128 pixel. The mit::dendra2 signal was automatically
584 thresholded (Otsu method), and all pixel *x* and *y* coordinates were extracted. The variance of x
585 and y coordinates was calculated and summed (*x+y* variance). For each condition, an average
586 of nine cell bodies were analysed and the mean *x+y* variance was calculated and expressed as
587 percent of control to obtain a mitochondrial distribution index. The same approach was used
588 for ER distribution based on KDEL::GFP signal.
589

590 **Manders' correlation between ER and mitochondria staining**

591 Confocal images of motor neuron of *OK371-GAL4, UAS-KDEL::GFP,UAS-mit::mKate2/UAS-*
592 *HA::Marf* third instar larvae were automatically treated to remove background on each channel
593 (Fiji, rolling ball method). Manders' correlation coefficient between mit::mKate2
594 (mitochondria) and KDEL::GFP (ER) signals was then determined (Fiji, Coloc2 plugin).
595

596 **NMJ mitochondrial content**

597 NMJ Z-stacks were treated using Fiji to create Z-projections (maximum intensity) and perform
598 an automatic threshold of the mit::dendra2 and myr::mRFP channels (Otsu method). The

599 integrated pixel density, that is an expression of the area on binary images, was calculated for
600 each bouton in each of the channel. The integrated density ratio, corresponding to the ratio of
601 the mitochondria area over the bouton area, was calculated. On average a hundred NMJ boutons
602 were analysed in each condition.
603
604 **Correlograms**
605 Using the *cor* function from the R package stats version 4.1.3, we calculated the Kendall
606 correlation coefficient between each quantitative variable. We chose the Kendall correlation
607 coefficient over Pearson or Spearman because it is not parametric and avoid any assumptions
608 about the data distribution. Then, these coefficients were plotted using the *corrplot* function
609 from the R package *corrplot version 0.92* (https://github.com/taiyun/corrplot).
610
611 **Code availability**
612 The code used to generate the results is available in our Github repository
613 **(**https://github.com/cedricmaurange/Varuk-et-al.git**)**
614
615 **Antibodies for western blots**
616 Primary antibodies: rabbit anti-Marf (gift from Alex Whitworth) (Ziviani et al., 2010) (1/1,000),
617 rat anti-HA (Roche, clone 3F10) (1/1,000), rat anti-α-Tubulin (Abcam, Ab6160) (1/10,000),
618 mouse anti-Ubiquitin (Merck, clone FK2) (1/500). Secondary HRP-coupled antibodies: rabbit
619 anti-rat (Jackson, 312-005-003), donkey anti-mouse (Jackson, 715-036-151), mouse anti-rabbit
620 (Jackson, 211-032-171) (all at 1/20,000).
621
622 **CNS protein extraction**
623 Five third instar larva CNS were dissected, immediately immersed into 20 µL of Laemmli
624 buffer containing 1mM DTT and protease inhibitors (Complete, Roche), heated 20 min at 70°C,
625 vigorously vortexed and stored at -20°C. Prior loading, protein samples were heated at 95°C
626 for 5 min.
627
628 **Immunoprecipitation**
629 Twenty five third instar larva CNS expressing HA::Marf were immersed in 100 µL of cold lysis
630 buffer (PBS, 0.1% NP40, Complete protease inhibitor from Roche and 1mM DTT) and frozen
631 in liquid nitrogen. The operation was repeated three times to obtain 75 CNS. The samples were
632 rapidly thawed at 37°C and snap frozen in liquid nitrogen three times, and then pooled and

633 homogenised using a 1 mL glass grinder and a tight Teflon pestle. The resulting suspension
634 was centrifuged twice at 800 g and the supernatant frozen at -80°C before immunoprecipitation
635 (IP). For IP, the sample was incubated 2 h at 4°C with rat anti-HA antibody (Roche, clone 3F10)
636 (1/40). Protein G-coupled magnetic beads (Dynabeads, Thermo Fisher) were incubated for 45
637 min at 4°C with rabbit anti-rat antibody (Jackson, 312-005-003) (1/20) and then mixed with the
638 HA-conjugated protein sample for 30 min at 4°C. The beads were washed according to
639 manufacturer instructions and immunoprecipitated HA::Marf was recovered following a 10 min
640 incubation at 95°C in 6X Laemmli sample buffer containing 5% of freshly added β-
641 mercaptoethanol.
642
643 **Western Blotting**
644 Proteins were separated on a 10% polyacrylamide gel in the presence of SDS at 100V. Transfer
645 was done at 100V for 1.5 h either on nitrocellulose membrane for larval CNS samples, or on
646 ethanol activated PVDF (0.45 µm) membrane for IP samples in 25mM tris-base, 190mM
647 glycine supplemented with ethanol (20% for nitrocellulose, 10% for PVDF). For anti-Ubiquitin
648 staining on IP samples, PVDF membranes were boiled after transfer for 10 min in distilled
649 water (Emmerich and Cohen, 2015). Blots were saturated in 5% BSA in PBS Tween20 0.05%
650 (PBT), probed with primary antibody and corresponding HRP-coupled secondary antibodies
651 with washing steps performed in PBT. Signal was revealed with chemiluminescent substrate
652 (SuperSignal West Pico Plus for anti-HA and Atto for anti-Ubiquitin, Thermo Fisher) and
653 images were acquired with a Bio-Rad imager. Blots of IP samples labelled with anti-Ubiquitin
654 were stripped 7 min in Restore WB Stripping Buffer (Thermo Scientific), washed and relabelled
655 with anti-HA. Band pixel intensities were measured using ImageJ (gel analysis plugin) and
656 quantification were performed on at least three independent blots with independent samples. α-
657 Tubulin was used for normalisation.
658
659
660
661
662
663
664
665

Acknowledgements

We thank Jean-Pierre Duneau (LISM, Marseille) for sharing his expertise on protein structure modelling and the IBDM microscopy and fly facilities for technical support. The IBDM-PiCsL platform is supported by ANR for the future program (France-BioImaging, ANR-10-877 INSB-04-01). We are grateful to Alice Corbet, Elisa Montredon and Carole Rubio for technical involvement. Experimental expenses, OOV's PhD fellowship, AR and CR's salaries, and CO and AC's internships were founded by the Association Française contre les Myopathies (AFM-Téléthon) (grant 22241 and 20097 to TR and fellowship 22070 and 23855 to OOV). We thank Lydia Kerkerian-Le Goff for scientific advices, and Laurent Kodjabachian and Pascale Durbec for supporting OOV's PhD completion with IBDM funding. Stocks from the Bloomington Drosophila Stock Center were used (NIH P40OD018537).

Author contribution

Project conception, supervision: TR. Experiment design: OOV, TR. Confocal, EM imaging: OOV, TR. Image analysis: OOV, TR, AC, AR. Lethality, locomotion, neurodegeneration: CO, AC. Biochemistry: OOV, TR. Fly genetics: OOV, AR, TR. Molecular biology: AR, OOV. EM samples: AA. Clustering, correlation: PdB. Lab logistics: AR, OOV. Manuscript: TR, OOV.

Disclosure and competing interests statement

The authors declare no competing interest.

Figures

699 **Figure 1. Hotspots of CMT2A mutations in MFN2.**

700 **(A)** Model of human MFN2 structure predicted by homology modelling based on BDLP (aa
701 1- 23 removed). Spheres: carbon α of the residues mutated in CMT2A. **(B)** Highlight on the
702 GD (front view) from MFN2 protein structure model. **(C)** Model of open MFN2 structure
703 (based on BDLP). Colour coding: proportion of aa mutated in CMT2A within a 10 aa interval.
704 Arrows indicate the most affected secondary structures. **(D)** CMT2A mutation frequency in
705 MFN2 closed conformation (model based on BDLP). **(E)** CMT2A mutation frequency in
706 MFN2 GD (front view). **(F)** MFN2 open (left) and closed (right) conformation models based
707 on BDLP showing the residues mutated in CMT2A that were selected for our study in flies.
708 The spheres represent the different atoms of the lateral chains (excluding hydrogen atoms).
709 Colour code refers to MFN2 domains. Putative localisation of the selected CMT2A residues is
710 based on their lateral chain orientation and environment.

711
712
713
714
715
716
717
718
719
720
721
722
723
724
725
726
727
728
729
730
731
732

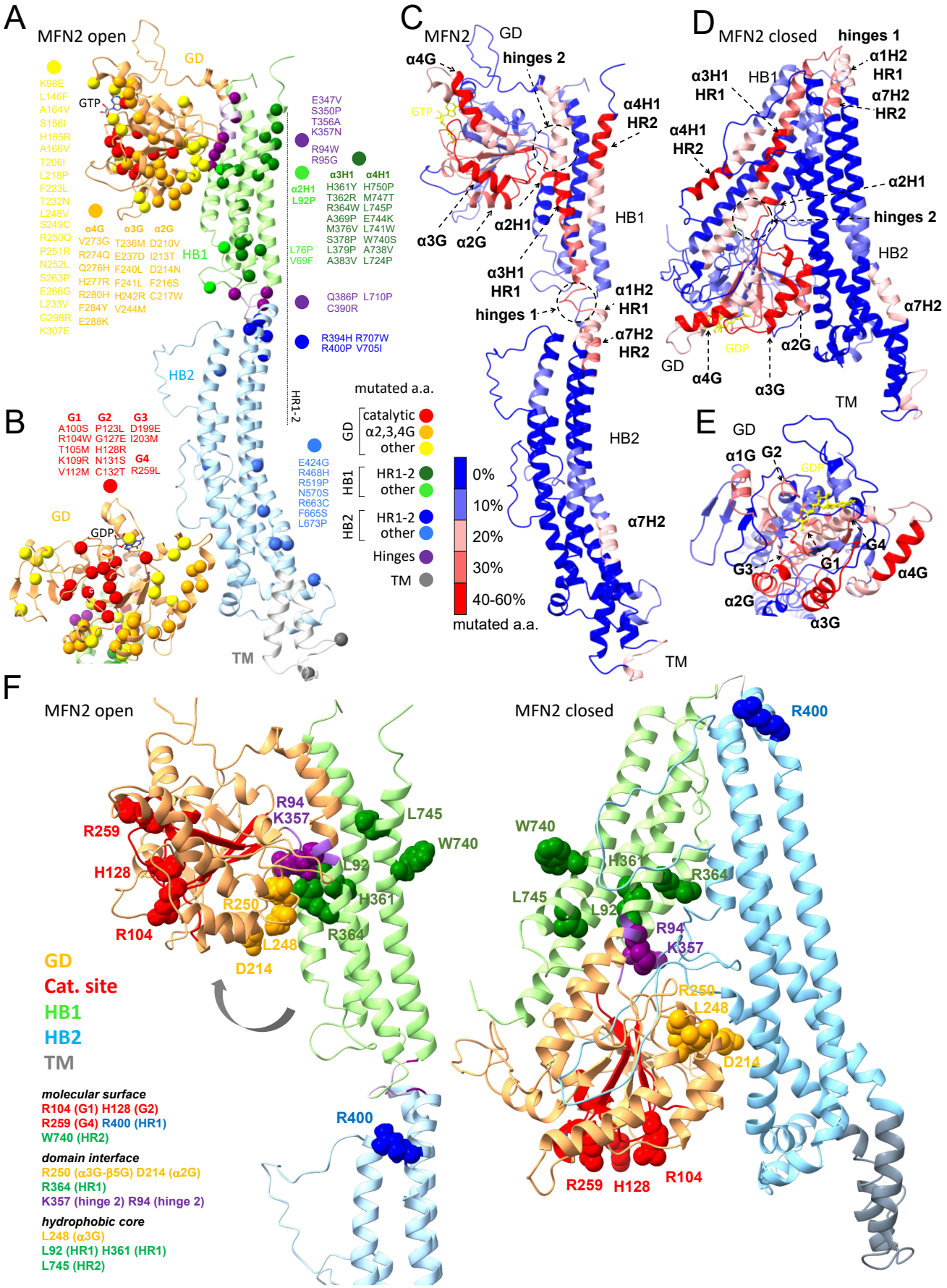
A
MFN2 open
GD
GTP
HB1
HB2
HR1-2
TM
K98E
L146F
A164V
S156I
H165R
A166V
T206I
L218P
F223L
T232N
L248V
S249C
R250Q
P251R
N252L
S263P
E266G
L233V
G298R
K307E
α4G
V273G
R274Q
Q276H
H277R
R280H
F284Y
E288K
α3G
T236M
E237D
F240L
F241L
H242R
V244M
α2G
D210V
I213T
D214N
F216S
C217W
E347V
S350P
T356A
K357N
R94W
R95G
α2H1
L92P
α3H1
H361Y
T362R
R364W
A369P
M376V
S378P
L379P
A383V
α4H1
H750P
M747T
L745P
E744K
L741W
W740S
A738V
L724P
L76P
V69F
Q386P
C390R
L710P
R394H
R400P
R707W
V705I
E424G
R468H
R519P
N570S
R663C
F665S
L673P
mutated a.a.
GD
catalytic
α2,3,4G
other
HB1
HR1-2
other
HB2
HR1-2
other
Hinges
TM
0%
10%
20%
30%
40-60%
mutated a.a.
B
G1
A100S
R104W
T105M
K109R
V112M
G2
P123L
G127E
H128R
N131S
C132T
G3
D199E
I203M
G4
R259L
GDP
C
MFN2
GD
hinges 2
α4G
GTP
α4H1
HR2
α2H1
α3G
α2G
HB1
α3H1
HR1
α1H2
HR1
hinges 1
α7H2
HR2
HB2
α7H2
TM
D
MFN2 closed
hinges 1
α1H2
HR1
α7H2
HR2
α3H1
HR1
HB1
α4H1
HR2
α2H1
hinges 2
HB2
α7H2
GDP
α2G
GD
α4G
α3G
TM
E
GD
α1G
G2
GDP
G4
G3
G1
α4G
α2G
α3G
F
MFN2 open
R94
K357
L745
W740
R259
H128
L92
R250
H361
R104
R364
L248
D214
GD
Cat. site
HB1
HB2
TM
molecular surface
R104 (G1) H128 (G2)
R259 (G4) R400 (HR1)
W740 (HR2)
domain interface
R250 (α3G-β5G) D214 (α2G)
R364 (HR1)
K357 (hinge 2) R94 (hinge 2)
hydrophobic core
L248 (α3G)
L92 (HR1) H361 (HR1)
L745 (HR2)
R400
MFN2 closed
R400
W740
H361
R364
L745
L92
R94
K357
R250
L248
D214
R259
H128
R104

Figure 1

733 **Figure 2. CMT2A alleles differently alter mitochondrial shape and organisation.**
734 **(A)** Dendrogram based on hierarchical clustering of mitochondrial morphology in wild-type
735 and *Marf*^{KO} backgrounds. Hydrophobic core: aa lateral chain pointing toward the inside and
736 associated with a network of hydrophobic residues. Molecular surface: aa lateral chain pointing
737 toward the surface of the molecule. Domain interface: aa lateral chain in a given domain
738 pointing toward another domain. **(B)** Confocal Airyscan image Z-projections (20 slices) of
739 mitochondrial networks from living motor neurons (ventral nerve cord, dorsal clusters) of third
740 instar larva (*OK371-GAL4, UAS-mit::dendra2)*. Colour code: Z-depth in dorso-ventral axis.
741 Wild type: flies with no *UAS-Marf* transgene. *Marf* ^{CTRL}: *UAS-HA::Marf* ^{WT}. Grape (*dR104W*),
742 Tangle (*dL92P*), Bulb (*dK357N*), Peanut (*dL745P*): *UAS-HA::Marf* ^{CMT2A}. Arrows highlight
743 mitochondrial morphological traits shown at higher magnification in the optic slices of bottom
744 panel: tubular and fragmented (wild type and Peanut), net-like (*Marf* ^{CTRL}), clustered and
745 fragmented (Grape), clustered and filamentous (Tangle), enlarged (Bulb). TEM mitochondria
746 high magnification views in motor neurons (dorsal clusters) from ventral nerve cord of third
747 instar larvae (*OK371-GAL4, UAS-mit::dendra2*). **(C)** Confocal Airyscan Z-projections (20
748 slices) of mitochondria from motor neurons (ventral nerve cord, dorsal clusters) of male *Marf*
749 ^{KO}*/Y, 3xP3-mCherry* ; *OK371-GAL4, UAS-mit::dendra2*. *Marf* ^{CTRL}: *UAS-HA::Marf* ^{WT}. Grape
750 (*dR104W*), Tangle (*dL92P*), Bulb (*dK357N*), Peanut (*dR250Q*): *UAS-HA::Marf* ^{CMT2A}. Colour
751 code: Z-depth, dorso-ventral axis. Arrows: regions shown at high magnification in the bottom
752 panels. **(D)** Mit::dendra2 photoconversion (non-photoconverted in green and photoconverted in
753 magenta) in living motor neurons (ventral nerve cord, dorsal clusters) from *OK371-GAL4, 2x*
754 *UAS-mit::dendra2/UAS-Marf* third instar larvae. Pictures show first and last snap shots of a 3
755 min movie. White circle: position of the photoconvertion beam. **(E)** Mean diffusion index
756 corresponding to the ratio of final area containing photoconverted dendra2 over initial
757 photoconverted area +/- SD. Mann-Whitney (MW) U test: p-value <0.05/*, p-value <0.01/**,
758 non-significant/ns.
759
760
761
762
763
764
765
766

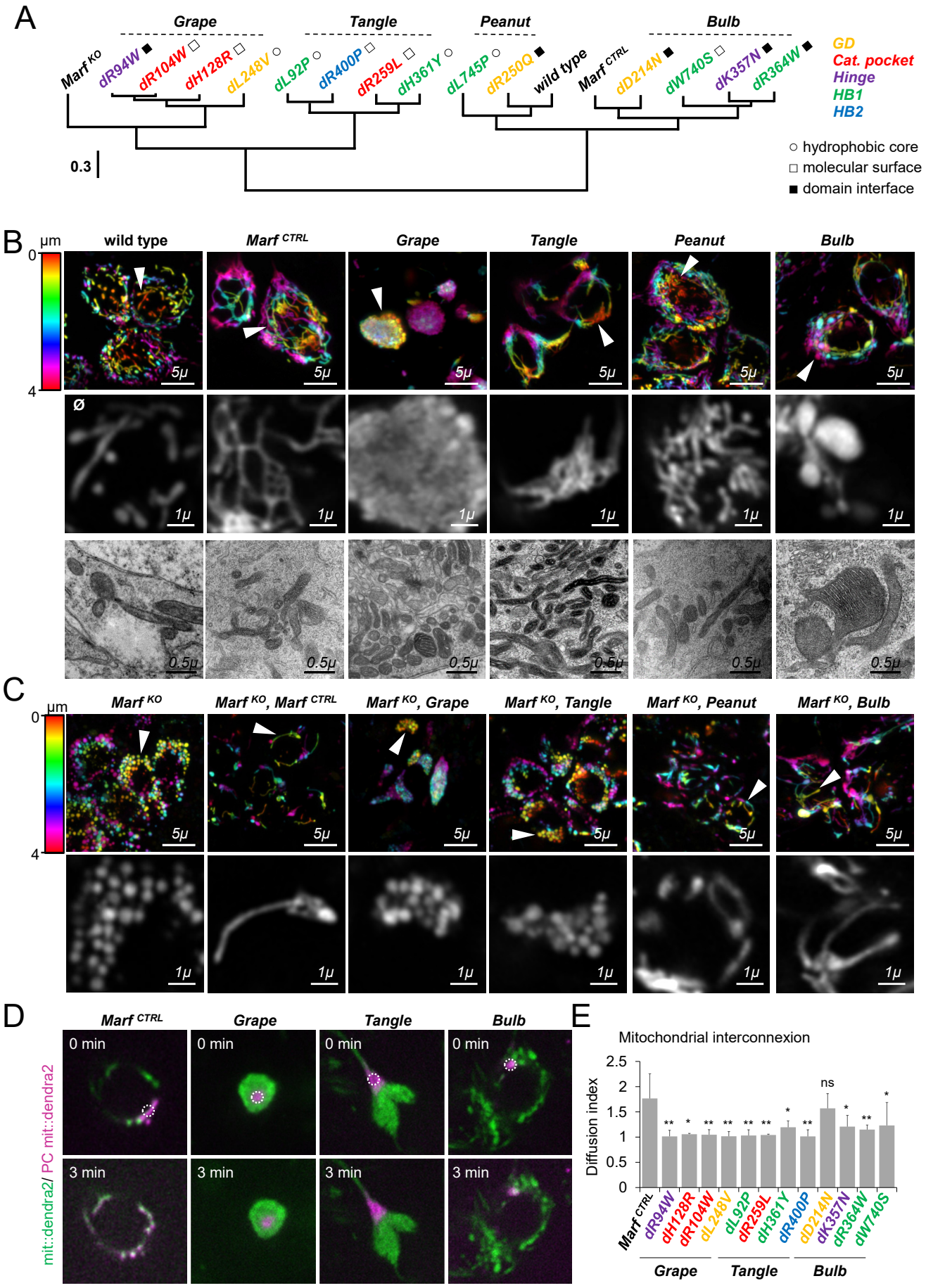
A
Grape
Tangle
Peanut
Bulb
Marf KO
dR94W
dR104W
dH128R
dL248V
dL92P
dR400P
dR259L
dH361Y
dL745P
dR250Q
wild type
Marf CTRL
dD214N
dW740S
dK357N
dR364W
GD
Cat. pocket
Hinge
HB1
HB2
0.3
hydrophobic core
molecular surface
domain interface
B
µm
0
4
wild type
Marf CTRL
Grape
Tangle
Peanut
Bulb
5µ
1µ
0.5µ
C
Marf KO
Marf KO, Marf CTRL
Marf KO, Grape
Marf KO, Tangle
Marf KO, Peanut
Marf KO, Bulb
D
Marf CTRL
Grape
Tangle
Bulb
0 min
3 min
mit::dendra2/ PC mit::dendra2
E
Mitochondrial interconnexion
Diffusion index
2.5
2
1.5
1
0.5
0
ns
Marf CTRL
dR94W
dH128R
dR104W
dL248V
dL92P
dR259L
dH361Y
dR400P
dD214N
dK357N
dR364W
dW740S
Grape
Tangle
Bulb

Figure 2

767 **Figure 3. Quantitative analysis of mitochondrial networks in CMT2A mutants.**
768 **(A)** Quantifications of mitochondrial morphology in larval motor neurons based on confocal
769 Airyscan image analysis. A given cell can contain one or several morphological traits:
770 fragmented, clustered, filamentous, net-like, enlarged. At least three individuals analysed per
771 conditions. On average twelve motor neurons scored per conditions (minimum: seven cells).
772 **(B)** Distribution of mitochondria (% of total mitochondria) in $Marf^{KO}$ larvae according to their
773 length (µm). AL: average length (µm). At least 3 individuals analysed with an average total of
774 338 mitochondria (minimum: 167). MW U test versus $Marf^{KO}$ p-value <0.05/*, p-value
775 <0.001/***. Colour code correspond to protein domains (see Figure 1F).
776
777
778
779
780
781
782
783
784
785
786
787
788
789
790
791
792
793
794
795
796
797
798
799
800

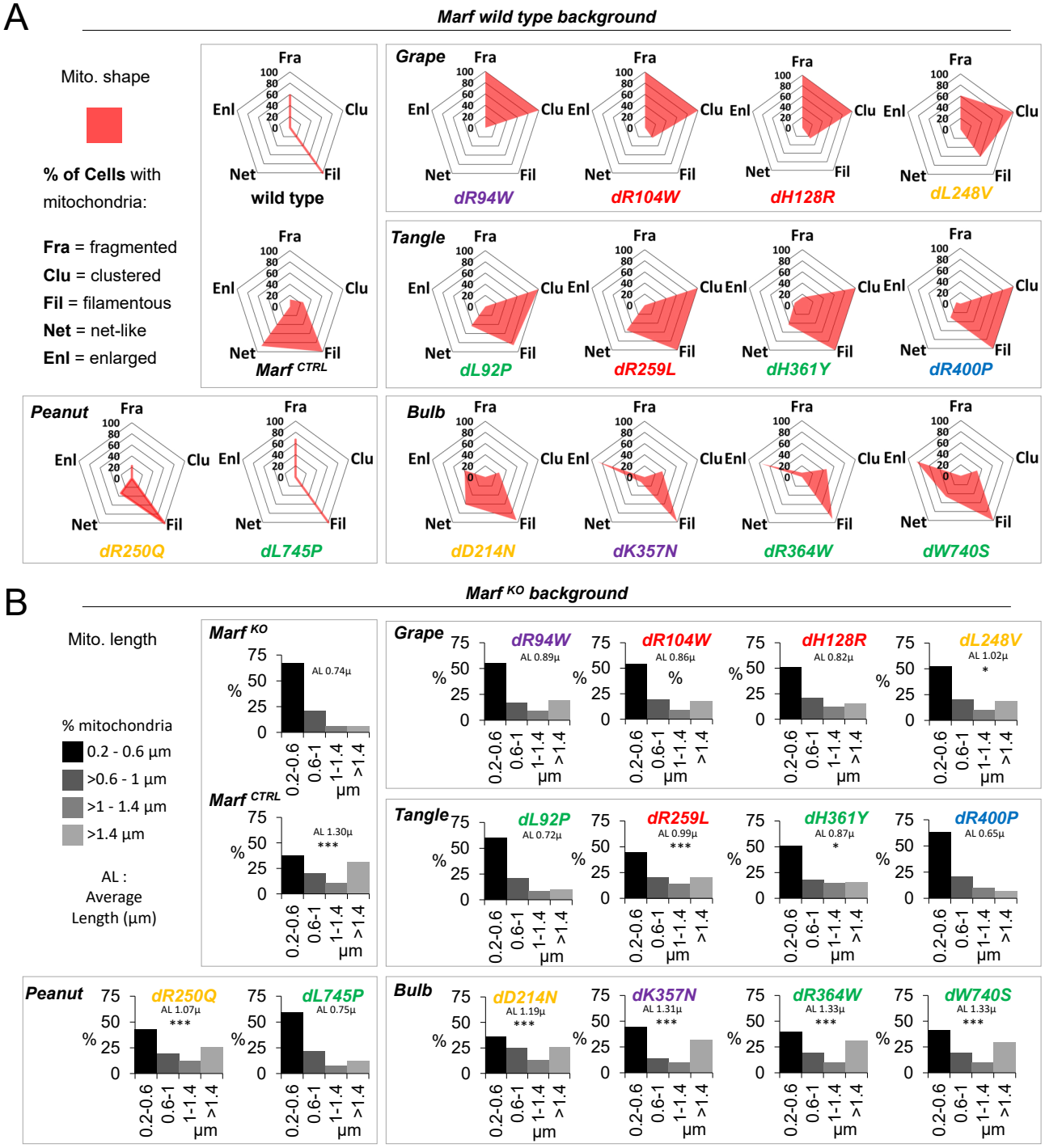
A
Marf wild type background
Mito. shape
% of Cells with mitochondria:
Fra = fragmented
Clu = clustered
Fil = filamentous
Net = net-like
Enl = enlarged
wild type
Marf CTRL
Grape
dR94W
dR104W
dH128R
dL248V
Tangle
dL92P
dR259L
dH361Y
dR400P
Peanut
dR250Q
dL745P
Bulb
dD214N
dK357N
dR364W
dW740S
B
Marf KO background
Mito. length
% mitochondria
0.2 - 0.6 µm
>0.6 - 1 µm
>1 - 1.4 µm
>1.4 µm
AL : Average Length (µm)
Marf KO
AL 0.74µ
Marf CTRL
AL 1.30µ
***
Grape
dR94W AL 0.89µ
dR104W AL 0.86µ
dH128R AL 0.82µ
dL248V AL 1.02µ
*
Tangle
dL92P AL 0.72µ
dR259L AL 0.99µ
***
dH361Y AL 0.87µ
*
dR400P AL 0.65µ
Peanut
dR250Q AL 1.07µ
***
dL745P AL 0.75µ
Bulb
dD214N AL 1.19µ
***
dK357N AL 1.31µ
***
dR364W AL 1.33µ
***
dW740S AL 1.33µ
***
0.2-0.6
0.6-1
1-1.4
>1.4
µm

Figure 3

801 **Figure 4. Varying degrees of neurotoxicity between CMT2A alleles.**
802 **(A)** Frequency of adult fly emergence *UAS-Marf* (*Marf* ^{CTRL} or *Marf* ^{CMT2A}) flies with or without
803 *elav-GAL4* driver (average of 380 flies analysed per condition, 3 independent experiments)
804 ranked in each allelic group according to decreasing phenotypic strength. Dashed line: expected
805 Mendelian frequency. ☺: moderate CMT2A or semi-dominant. **(B)** Average proportion of
806 ommatidia containing less than seven visible photoreceptor rhabdomeres +/- SEM in the retina
807 of one week old *elav-GAL4 ; UAS-mit::dendra2/UAS-Marf* (*Marf* ^{CTRL} or *Marf* ^{CMT2A}) adult flies
808 ranked by allelic groups according to decreasing phenotypic strength. Images: ommatidia with
809 seven or less than seven photoreceptors. On average 175 ommatidia analysed from eight
810 individuals per condition. MW U test: p-value <0.05/*, p-value <0.01/**, p-value <0.001/***.
811 ☺: moderate CMT2A or semi-dominant. **(C)** Average locomotor performance (startle-induced
812 negative geotaxis) of ten days old *elav-GAL4 ; UAS-mit::dendra2/UAS-Marf* (*Marf* ^{CTRL} or
813 *Marf* ^{CMT2A}) adult flies. Histogram shows the proportion of flies according to the height they
814 have reached (1: 0-15 mm, 2: >15-30 mm, 3: >30-45mm, 4: >45mm). Mean of 3-4 independent
815 races involving 20-30 flies. MW U test: p-value <0.05/*, p-value <0.01/**, p-value <0.001/***,
816 non-significant/ns. ☺: moderate CMT2A or semi-dominant. Colour code correspond to protein
817 domains (see Figure 1F).
818
819
820
821
822
823
824
825
826
827
828
829
830
831
832
833

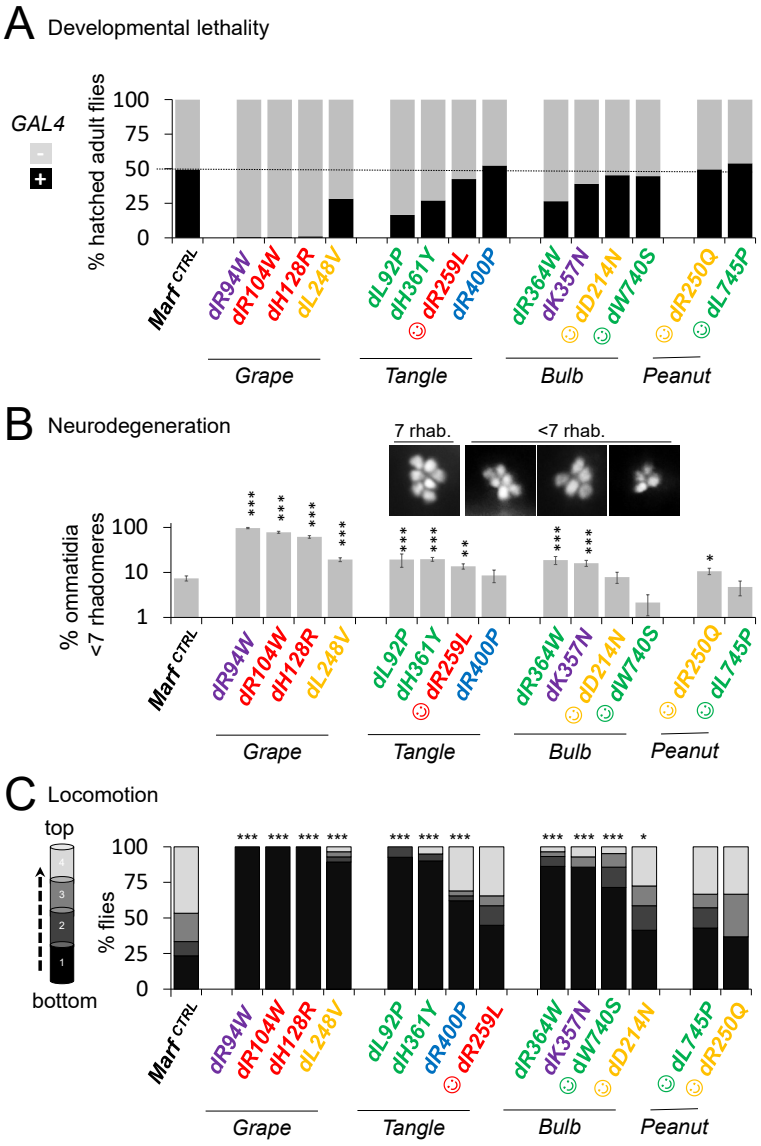
A Developmental lethality
GAL4
-
+
% hatched adult flies
100
75
50
25
0
Marf CTRL
dR94W
dR104W
dH128R
dL248V
dL92P
dH361Y
dR259L
dR400P
dR364W
dK357N
dD214N
dW740S
dR250Q
dL745P
Grape
Tangle
Bulb
Peanut
B Neurodegeneration
7 rhab.
<7 rhab.
% ommatidia <7 rhadomeres
100
10
1
C Locomotion
top
bottom
% flies
100
75
50
25
0

Figure 4

834 **Figure 5. Alterations of mitochondrial distribution correlates with neurotoxicity.**
835 **(A)** Confocal microscopy of living motor neurons showing mitochondria and plasma membrane
836 in *OK371-GAL4, UAS-mit::dendra2 ; UAS-myr::mRFP* third instar larva expressing *Marf* ^{CTRL}
837 and *Marf* ^{CMT2A} *(dL92P*). **(B)** Mean mitochondrial distribution index +/- SD. Variance of all
838 mitochondrial pixel coordinates (x, y) was analysed on average on nine cell bodies. MW U test:
839 p-value <0.05/*, p-value <0.01/**, p-value <0.001/***. **(C)** Confocal Airyscan microscopy
840 images of living motor neurons showing mitochondria and ER in *OK371-GAL4, UAS-*
841 *mit::mKate2, UAS-KDEL::GFP* third instar larva expressing *Marf* ^{CTRL} and *Marf* ^{CMT2A}
842 *(dL92P*). Magnification views: ER and mitochondria in close vicinity and overlapping (arrow
843 heads). **(D)** Mean distribution index of endoplasmic reticulum for the different CMT2A alleles
844 +/- SD. At least, three cell bodies analysed per condition. MW U test: not significant. **(E)**
845 Histogram showing mean Manders' coefficient (percent of *Marf* ^{CTRL}) representing the fraction
846 of KDEL::GFP (ER) signal overlapping with mit::mKate2 (mitochondria) staining +/- SD (sum
847 of GFP pixel intensities with mKate2 intensity above 0 divided by the total GFP pixel intensity).
848 Average image number analysed: 19 (minimum 14). MW U test: p-value <0.05/*, p-value
849 <0.01/**, p-value <0.001/***. **(F)** Mean Manders' coefficients (percent of *Marf* ^{CTRL})
850 representing the fraction of mit::mKate2 (mitochondria) signal overlapping with KDEL::GFP
851 (ER) staining +/- SD (sum of mKate2 pixel intensities with GFP intensity above 0 divided by
852 the total mKate2 pixel intensity). Average image number analysed: 19 (minimum 14). MW U
853 test: p-value <0.05/*, p-value <0.01/**, p-value <0.001/***. **(G)** Confocal Airyscan
854 microscopy images showing mitochondria within NMJ boutons in living muscles from *OK371-*
855 *GAL4, UAS-mit::dendra2 ; UAS-myr::mRFP* third instar larva expressing *Marf* ^{CTRL} and *Marf*
856 ^{CMT2A} *(dL92P*). Insight: high magnification view of synaptic boutons. **(H)** Mean ratio of
857 mitochondrial over bouton area +/- SD. Average boutons analysed: 100). MW U test: p-value
858 <0.05/*, p-value <0.01/**, p-value <0.001/***. **(I)** Correlation plot between mitochondrial
859 distribution in motor neuron soma (data Figure 5A) and locomotor performances (data Figure
860 4C) both expressed as percent of *Marf* ^{CTRL}. τ: Kendall correlation coefficient. p: p-value.
861
862
863
864
865
866
867

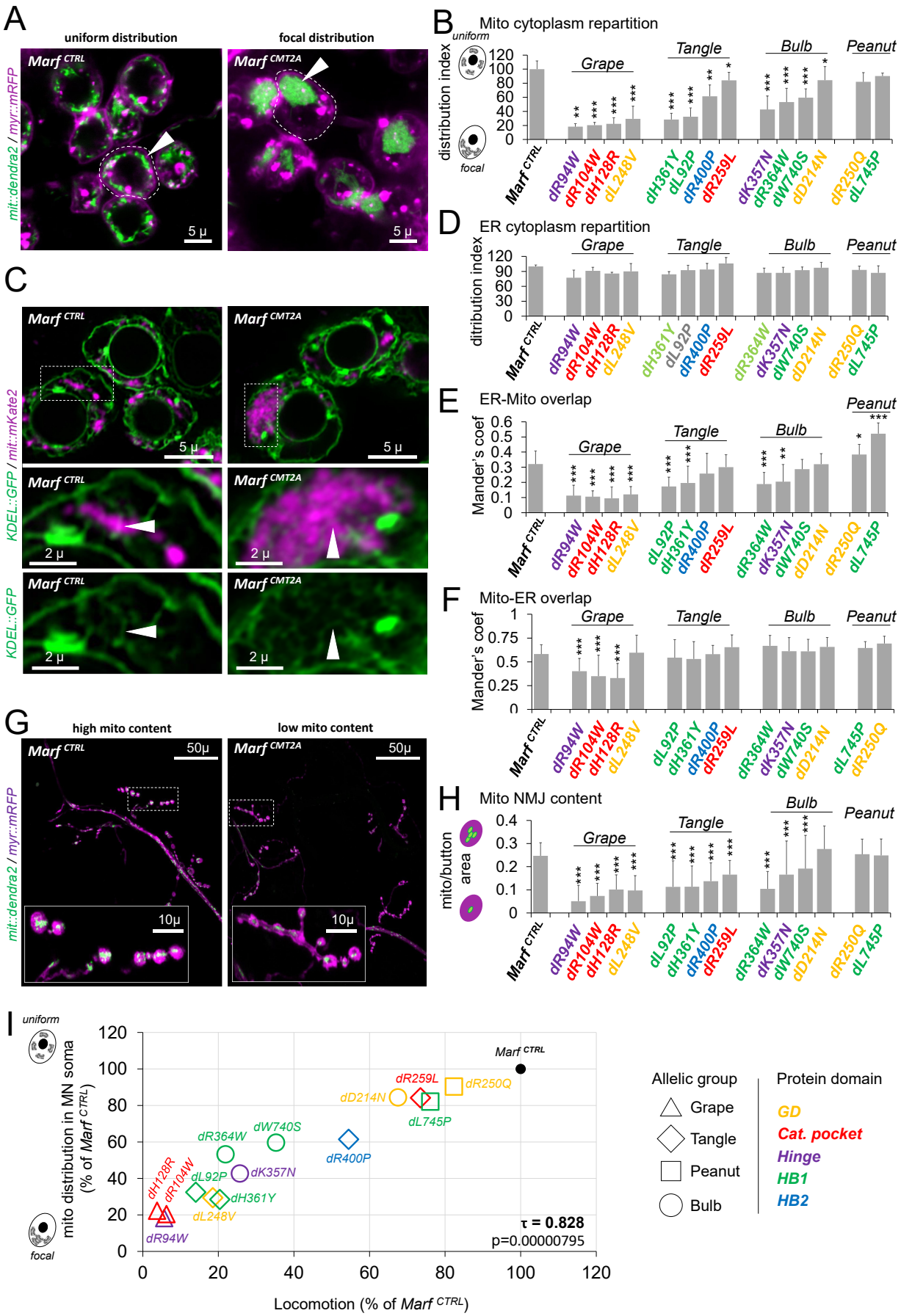
A
uniform distribution
focal distribution
mit::dendra2 / myr::mRFP
Marf CTRL
Marf CMT2A
5 µ
B
Mito cytoplasm repartition
distribution index
uniform
focal
Grape
Tangle
Bulb
Peanut
Marf CTRL
dR94W
dR104W
dH128R
dL248V
dH361Y
dL92P
dR400P
dR259L
dK357N
dR364W
dW740S
dD214N
dR250Q
dL745P
C
KDEL::GFP / mit::mKate2
KDEL::GFP
2 µ
D
ER cytoplasm repartition
ditribution index
E
ER-Mito overlap
Mander's coef
F
Mito-ER overlap
G
high mito content
low mito content
mit::dendra2 / myr::mRFP
50µ
10µ
H
Mito NMJ content
mito/button area
I
mito distribution in MN soma (% of Marf CTRL)
Locomotion (% of Marf CTRL)
τ = 0.828
p=0.00000795
Allelic group
Grape
Tangle
Peanut
Bulb
Protein domain
GD
Cat. pocket
Hinge
HB1
HB2

Figure 5

868 **Figure 6. Most CMT2A alleles are insensitive to Parkin overexpression.**
869 **(A)** Confocal Airyscan images from living motor neuron of *OK371-GAL4, UAS-mit::dendra2/*
870 *UAS-parkin* (*parkin*^{OE}) third instar larva expressing *Marf*^{CTRL} or *Marf*^{CMT2A}. The mitochondrial
871 structures pinpointed by arrows are magnified on bottom panel images. Grape: *dR94W*. Tangle:
872 *dL92P*. Peanut: *dL745P*. Bulb: *dR364W*. **(B)** Quantifications of mitochondrial morphology in
873 larval motor neurons overexpressing Parkin (*parkin*^{OE}) based on confocal Airyscan image
874 stacks. A given cell can contain mitochondria with one or several morphological traits:
875 fragmented, clustered, filamentous, net-like, enlarged. Black lines: phenotypes without
876 *parkin*^{OE}. Red surfaces: phenotype upon *parkin*^{OE}. At least three individuals were analysed.
877 Average total number of motor neurons analysed: 11 (minimum 6). **(C)** Developmental lethality
878 with (+) or without (-) *parkin* overexpression (*parkin*^{OE}). Males *elav-GAL4/Y ; UAS-*
879 *mit::dendra2* flies were crossed to *UAS-parkin* females combined with *UAS-Marf*^{CTRL} *or UAS-*
880 *Marf*^{CMT2A} and were kept at 29°C. In the resulting adult progeny, the number of males (no *elav-*
881 *GAL4*) and females (with *elav-GAL4*) was determined (average of 150 flies per conditions). To
882 minimize developmental lethality, *dR94W*, *dR104W* and *dH128R* were crossed to *OK371-*
883 *GAL4, UAS-mit::dendra2/CyO* and kept at 25°C. Flies with Curly and wild-type wings were
884 scored. Colour code correspond to protein domains (see Figure 1F). The difference in percent
885 between males and females, or Curly and non-Curly populations referred as percent survival.
886 The percent lethality corresponds to 100 minus the percent survival.
887
888
889
890
891
892
893
894
895
896
897
898
899
900
901

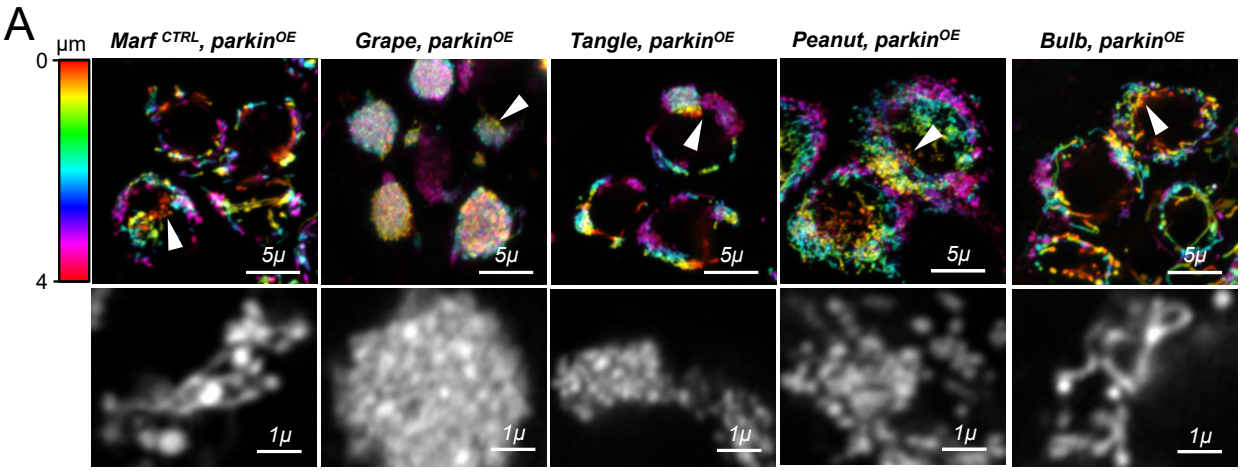
A
μm
0
4
Marf CTRL, parkinOE
Grape, parkinOE
Tangle, parkinOE
Peanut, parkinOE
Bulb, parkinOE
5μ
1μ

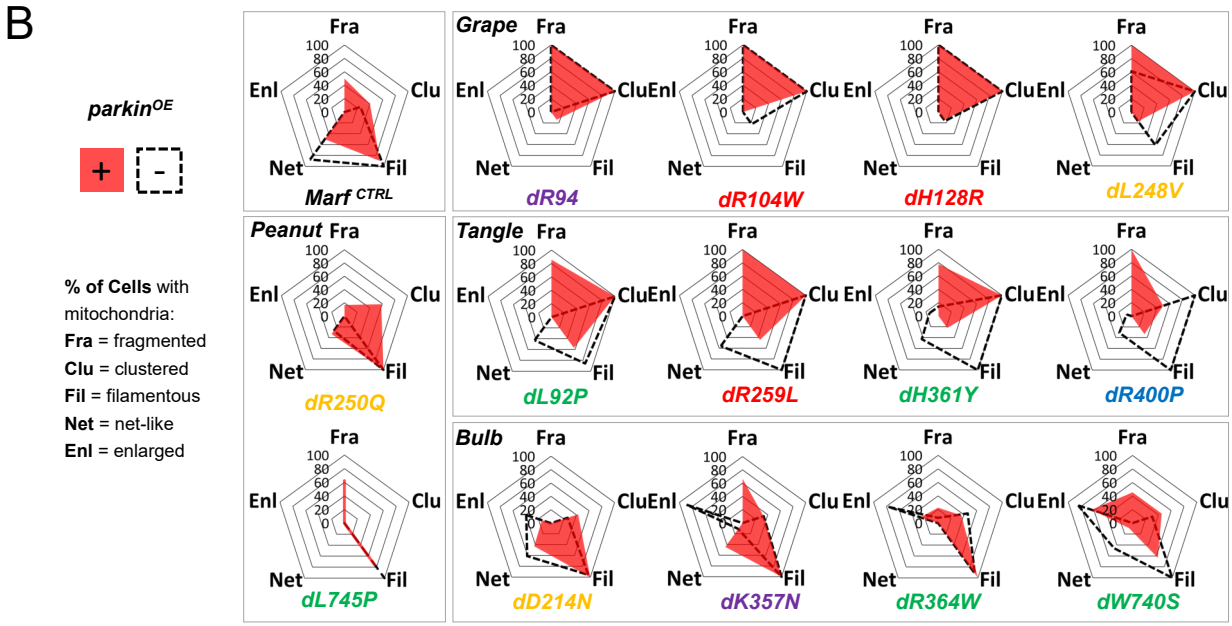
B
parkinOE
+
-
% of Cells with mitochondria:
Fra = fragmented
Clu = clustered
Fil = filamentous
Net = net-like
Enl = enlarged
Fra
Clu
Fil
Net
Enl
Marf CTRL
Grape
dR94
dR104W
dH128R
dL248V
Peanut
dR250Q
Tangle
dL92P
dR259L
dH361Y
dR400P
dL745P
Bulb
dD214N
dK357N
dR364W
dW740S

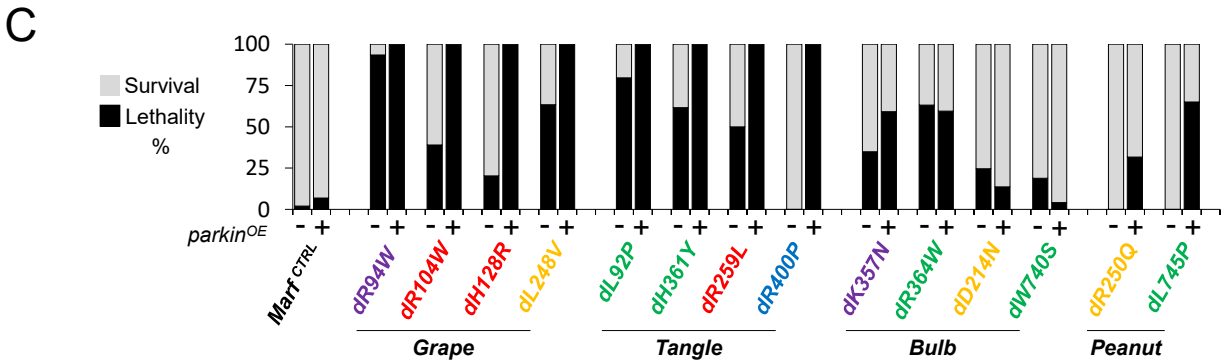
C
Survival
Lethality
%
100
75
50
25
0
parkinOE
- +
Marf CTRL
dR94W
dR104W
dH128R
dL248V
dL92P
dH361Y
dR259L
dR400P
dK357N
dR364W
dD214N
dW740S
dR250Q
dL745P
Grape
Tangle
Bulb
Peanut

Figure 6

902 **Figure 7. Decreased ubiquitination and increased protein level in CMT2A mutant Marf.**
903 **(A)** Anti-HA and anti-Ubiquitin western blots of immunoprecipitated wild-type HA-tagged
904 Marf (IP) from *elav-GAL4 ; UAS-mit::dendra2/UAS-HA::Marf* (*Marf* ^{CTRL}) third instar larva
905 CNS. Input: protein extract before IP. Same blot first stained with anti-Ubiquitin, and following
906 stripping, re-probed with anti-HA. Black arrows: ubiquitinated Marf. **(B)** Anti-HA western blot
907 of proteins from *elav-GAL4 ; UAS-mit::dendra2/UAS-HA::Marf* (*Marf* ^{CTRL}) larval CNS alone
908 (ø) or with *UAS-RNAi* against *parkin* (*parkin*^{KD}). Black arrows: ubiquitinated Marf. **(C)** Anti-
909 HA and anti-α-Tubulin western blot of proteins from CNS of *elav-GAL4 ; UAS-*
910 *mit::dendra2/UAS-HA::Marf* (*Marf* ^{CTRL} or *Marf* ^{CMT2A}) larvae. Black arrows: ubiquitinated
911 Marf. White arrow: native Marf. **(D)** Average ratio between ubiquitinated and native Marf
912 based on western blot signal analysis. Mean +/- SD of 3-4 experiments involving independent
913 samples (5 CNS). MW U test: p-value <0.05/*, p-value <0.01/**. **(E)** Average native Marf
914 level (arbitrary units) based on western signal intensity (normalisation: α-Tubulin). Mean +/-
915 SD of 3-4 experiments involving independent samples (5 CNS). MW U test: p-value <0.05/*,
916 p-value <0.01/**. Colour code correspond to protein domains (see Figure 1F).
917
918
919
920
921
922
923
924
925
926
927
928
929
930
931
932
933

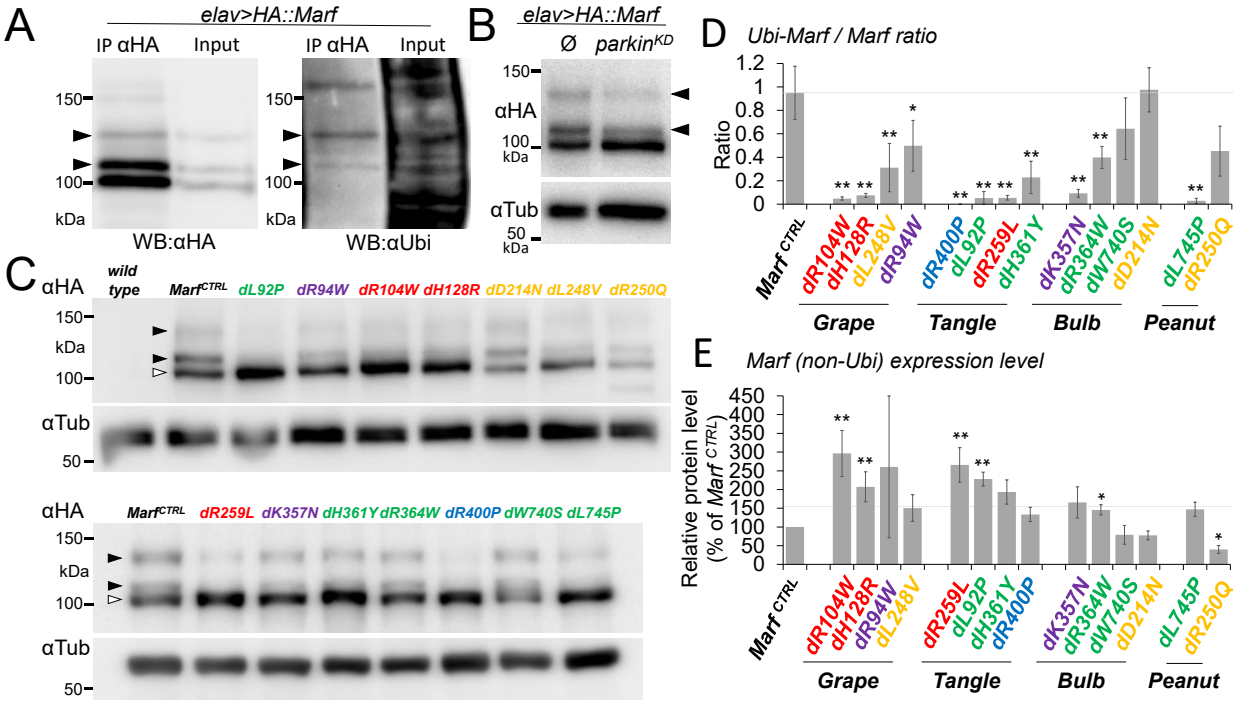
A
elav>HA::Marf
IP αHA
Input
IP αHA
Input
150
100
kDa
WB:αHA
WB:αUbi
B
elav>HA::Marf
Ø
parkinKD
αHA
αTub
C
wild type
MarfCTRL
dL92P
dR94W
dR104W
dH128R
dD214N
dL248V
dR250Q
dR259L
dK357N
dH361Y
dR364W
dR400P
dW740S
dL745P
αTub
50
D
Ubi-Marf / Marf ratio
Ratio
Grape
Tangle
Bulb
Peanut
E
Marf (non-Ubi) expression level
Relative protein level (% of MarfCTRL)

Figure 7

1318 # References

1319 Acevedo JM, Hoermann B, Schlimbach T, Teleman AA (2018) Changes in global translation elongation
1320 or initiation rates shape the proteome via the Kozak sequence. Scientific reports 8:4018.
1321 Ajroud-Driss S, Fecto F, Ajroud K, Yang Y, Donkervoort S, Siddique N, Siddique T (2009) A novel de
1322 novo MFN2 mutation causing CMT2A with upper motor neuron signs. Neurogenetics 10:359-
1323 361.
1324 Alsayyah C, Ozturk O, Cavellini L, Belgareh-Touze N, Cohen MM (2020) The regulation of
1325 mitochondrial homeostasis by the ubiquitin proteasome system. Biochim Biophys Acta
1326 Bioenerg 1861:148302.
1327 Alsayyah C, Singh MK, Morcillo-Parra MA, Cavellini L, Shai N, Schmitt C, Schuldiner M, Zalckvar E,
1328 Mallet A, Belgareh-Touze N, Zimmer C, Cohen MM (2024) Mitofusin-mediated contacts
1329 between mitochondria and peroxisomes regulate mitochondrial fusion. PLoS Biol
1330 22:e3002602.
1331 Amiott EA, Cohen MM, Saint-Georges Y, Weissman AM, Shaw JM (2009) A mutation associated with
1332 CMT2A neuropathy causes defects in Fzo1 GTP hydrolysis, ubiquitylation, and protein
1333 turnover. Molecular biology of the cell 20:5026-5035.
1334 Anton F, Fres JM, Schauss A, Pinson B, Praefcke GJ, Langer T, Escobar-Henriques M (2011) Ugo1 and
1335 Mdm30 act sequentially during Fzo1-mediated mitochondrial outer membrane fusion.
1336 Journal of cell science 124:1126-1135.
1337 Barsa C, Perrin J, David C, Mourier A, Rojo M (2025) A cellular assay to determine the fusion capacity
1338 of MFN2 variants linked to Charcot-Marie-Tooth disease of type 2 A. Scientific reports
1339 15:9971.
1340 Beresewicz M, Charzewski L, Krzysko KA, Kochanski A, Zablocka B (2018) Molecular modelling of
1341 mitofusin 2 for a prediction for Charcot-Marie-Tooth 2A clinical severity. Scientific reports
1342 8:16900.
1343 Bertholet AM, Delerue T, Millet AM, Moulis MF, David C, Daloyau M, Arnaune-Pelloquin L, Davezac
1344 N, Mils V, Miquel MC, Rojo M, Belenguer P (2016) Mitochondrial fusion/fission dynamics in
1345 neurodegeneration and neuronal plasticity. Neurobiology of disease 90:3-19.
1346 Brandner A, De Vecchis D, Baaden M, Cohen MM, Taly A (2019) Physics-based oligomeric models of
1347 the yeast mitofusin Fzo1 at the molecular scale in the context of membrane docking.
1348 Mitochondrion 49:234-244.
1349 Calvo J, Funalot B, Ouvrier RA, Lazaro L, Toutain A, De Mas P, Bouche P, Gilbert-Dussardier B, Arne-
1350 Bes MC, Carriere JP, Journel H, Minot-Myhie MC, Guillou C, Ghorab K, Magy L, Sturtz F, Vallat
1351 JM, Magdelaine C (2009) Genotype-phenotype correlations in Charcot-Marie-Tooth disease
1352 type 2 caused by mitofusin 2 mutations. Archives of neurology 66:1511-1516.
1353 Cao YL, Meng S, Chen Y, Feng JX, Gu DD, Yu B, Li YJ, Yang JY, Liao S, Chan DC, Gao S (2017) MFN1
1354 structures reveal nucleotide-triggered dimerization critical for mitochondrial fusion. Nature
1355 542:372-376.
1356 Cartoni R, Martinou JC (2009) Role of mitofusin 2 mutations in the physiopathology of Charcot-
1357 Marie-Tooth disease type 2A. Experimental neurology 218:268-273.
1358 Chen H, Chomyn A, Chan DC (2005) Disruption of fusion results in mitochondrial heterogeneity and
1359 dysfunction. The Journal of biological chemistry 280:26185-26192.
1360 Chen VB, Arendall WB, 3rd, Headd JJ, Keedy DA, Immormino RM, Kapral GJ, Murray LW, Richardson
1361 JS, Richardson DC (2010) MolProbity: all-atom structure validation for macromolecular
1362 crystallography. Acta Crystallogr D Biol Crystallogr 66:12-21.
1363 Chevrollier A, Cassereau J, Ferre M, Alban J, Desquiret-Dumas V, Gueguen N, Amati-Bonneau P,
1364 Procaccio V, Bonneau D, Reynier P (2012) Standardized mitochondrial analysis gives new
1365 insights into mitochondrial dynamics and OPA1 function. The international journal of
1366 biochemistry & cell biology 44:980-988.

1367 Codron P, Chevrollier A, Kane MS, Echaniz-Laguna A, Latour P, Reynier P, Bonneau D, Verny C,
1368 Procaccio V, Lenaers G, Cassereau J (2016) Increased mitochondrial fusion in a autosomal
1369 recessive CMT2A family with mitochondrial GTPase mitofusin 2 mutations. Journal of the
1370 peripheral nervous system : JPNS 21:365-369.
1371 Cohen MM, Amiott EA, Day AR, Leboucher GP, Pryce EN, Glickman MH, McCaffery JM, Shaw JM,
1372 Weissman AM (2011) Sequential requirements for the GTPase domain of the mitofusin Fzo1
1373 and the ubiquitin ligase SCFMdm30 in mitochondrial outer membrane fusion. Journal of cell
1374 science 124:1403-1410.
1375 Cohen MM, Leboucher GP, Livnat-Levanon N, Glickman MH, Weissman AM (2008) Ubiquitin-
1376 proteasome-dependent degradation of a mitofusin, a critical regulator of mitochondrial
1377 fusion. Molecular biology of the cell 19:2457-2464.
1378 Cuthbertson JM, Doyle DA, Sansom MS (2005) Transmembrane helix prediction: a comparative
1379 evaluation and analysis. Protein Eng Des Sel 18:295-308.
1380 Das R, Das S, Chakrabarti S, Chakrabarti O (2022a) CMT2A-linked mitochondrial hyperfusion-driving
1381 mutant MFN2 perturbs ER-mitochondrial associations and Ca(2+) homeostasis. Biol Cell
1382 114:309-319.
1383 Das R, Kamal IM, Das S, Chakrabarti S, Chakrabarti O (2022b) MITOL-mediated DRP1 ubiquitylation
1384 and degradation promotes mitochondrial hyperfusion in a CMT2A-linked MFN2 mutant.
1385 Journal of cell science 135.
1386 Das R, Maity S, Das P, Kamal IM, Chakrabarti S, Chakrabarti O (2024) CMT2A-linked MFN2 mutation,
1387 T206I promotes mitochondrial hyperfusion and predisposes cells towards mitophagy.
1388 Mitochondrion 74:101825.
1389 Daste F, Sauvanet C, Bavdek A, Baye J, Pierre F, Le Borgne R, David C, Rojo M, Fuchs P, Tareste D
1390 (2018) The heptad repeat domain 1 of Mitofusin has membrane destabilization function in
1391 mitochondrial fusion. EMBO reports 19.
1392 De Vecchis D, Brandner A, Baaden M, Cohen MM, Taly A (2019) A Molecular Perspective on
1393 Mitochondrial Membrane Fusion: From the Key Players to Oligomerization and Tethering of
1394 Mitofusin. J Membr Biol 252:293-306.
1395 Debattisti V, Pendin D, Ziviani E, Daga A, Scorrano L (2014) Reduction of endoplasmic reticulum stress
1396 attenuates the defects caused by Drosophila mitofusin depletion. The Journal of cell biology
1397 204:303-312.
1398 Detmer SA, Chan DC (2007) Complementation between mouse Mfn1 and Mfn2 protects
1399 mitochondrial fusion defects caused by CMT2A disease mutations. The Journal of cell biology
1400 176:405-414.
1401 El Fissi N, Rojo M, Aouane A, Karatas E, Poliacikova G, David C, Royet J, Rival T (2018) Mitofusin gain
1402 and loss of function drive pathogenesis in Drosophila models of CMT2A neuropathy. EMBO
1403 reports.
1404 Emmerich CH, Cohen P (2015) Optimising methods for the preservation, capture and identification of
1405 ubiquitin chains and ubiquitylated proteins by immunoblotting. Biochemical and biophysical
1406 research communications 466:1-14.
1407 Escobar-Henriques M, Joaquim M (2019) Mitofusins: Disease Gatekeepers and Hubs in Mitochondrial
1408 Quality Control by E3 Ligases. Front Physiol 10:517.
1409 Formosa LE, Ryan MT (2016) Mitochondrial fusion: Reaching the end of mitofusin's tether. The
1410 Journal of cell biology 215:597-598.
1411 Franco A, Kitsis RN, Fleischer JA, Gavathiotis E, Kornfeld OS, Gong G, Biris N, Benz A, Qvit N, Donnelly
1412 SK, Chen Y, Mennerick S, Hodgson L, Mochly-Rosen D, Dorn GW, II (2016) Correcting
1413 mitochondrial fusion by manipulating mitofusin conformations. Nature 540:74-79.
1414 Giacomello M, Pyakurel A, Glytsou C, Scorrano L (2020) The cell biology of mitochondrial membrane
1415 dynamics. Nature reviews Molecular cell biology 21:204-224.
1416 Goddard TD, Huang CC, Meng EC, Pettersen EF, Couch GS, Morris JH, Ferrin TE (2018) UCSF
1417 ChimeraX: Meeting modern challenges in visualization and analysis. Protein Sci 27:14-25.

1418 Gordaliza-Alaguero I, Canto C, Zorzano A (2019) Metabolic implications of organelle-mitochondria
1419 communication. EMBO reports 20:e47928.
1420 Gouy M, Tannier E, Comte N, Parsons DP (2021) Seaview Version 5: A Multiplatform Software for
1421 Multiple Sequence Alignment, Molecular Phylogenetic Analyses, and Tree Reconciliation.
1422 Methods Mol Biol 2231:241-260.
1423 Huo Y, Sun W, Shi T, Gao S, Zhuang M (2022) The MFN1 and MFN2 mitofusins promote clustering
1424 between mitochondria and peroxisomes. Commun Biol 5:423.
1425 Hwa JJ, Hiller MA, Fuller MT, Santel A (2002) Differential expression of the Drosophila mitofusin
1426 genes fuzzy onions (fzo) and dmfn. Mechanisms of development 116:213-216.
1427 Joaquim M, Bulimaga MB, Mohn MA, Plouzennec S, Osinski L, Altin S, Mahabir E, Chevrollier A,
1428 Escobar-Henriques M (2025) Charcot-Marie-Tooth type 2A variants of mitofusin 2 sensitize
1429 cells to apoptotic cell death. Journal of cell science 138.
1430 Jumper J, Evans R, Pritzel A, Green T, Figurnov M, Ronneberger O, Tunyasuvunakool K, Bates R, Zidek
1431 A, Potapenko A, Bridgland A, Meyer C, Kohl SAA, Ballard AJ, Cowie A, Romera-Paredes B,
1432 Nikolov S, Jain R, Adler J, Back T, Petersen S, Reiman D, Clancy E, Zielinski M, Steinegger M,
1433 Pacholska M, Berghammer T, Bodenstein S, Silver D, Vinyals O, Senior AW, Kavukcuoglu K,
1434 Kohli P, Hassabis D (2021) Highly accurate protein structure prediction with AlphaFold.
1435 Nature 596:583-589.
1436 Kageyama Y, Zhang Z, Roda R, Fukaya M, Wakabayashi J, Wakabayashi N, Kensler TW, Reddy PH,
1437 Iijima M, Sesaki H (2012) Mitochondrial division ensures the survival of postmitotic neurons
1438 by suppressing oxidative damage. The Journal of cell biology 197:535-551.
1439 Kawalec M, Zablocka B, Kabzinska D, Neska J, Beresewicz M (2014) Mitofusin 2 expression dominates
1440 over mitofusin 1 exclusively in mouse dorsal root ganglia - a possible explanation for
1441 peripheral nervous system involvement in Charcot-Marie-Tooth 2A. Folia Neuropathol
1442 52:436-442.
1443 Kijima K, Numakura C, Izumino H, Umetsu K, Nezu A, Shiiki T, Ogawa M, Ishizaki Y, Kitamura T,
1444 Shozawa Y, Hayasaka K (2005) Mitochondrial GTPase mitofusin 2 mutation in Charcot-Marie-
1445 Tooth neuropathy type 2A. Hum Genet 116:23-27.
1446 Koshiba T, Detmer SA, Kaiser JT, Chen H, McCaffery JM, Chan DC (2004) Structural basis of
1447 mitochondrial tethering by mitofusin complexes. Science 305:858-862.
1448 Li YJ, Cao YL, Feng JX, Qi Y, Meng S, Yang JF, Zhong YT, Kang S, Chen X, Lan L, Luo L, Yu B, Chen S, Chan
1449 DC, Hu J, Gao S (2019) Structural insights of human mitofusin-2 into mitochondrial fusion and
1450 CMT2A onset. Nat Commun 10:4914.
1451 Low HH, Lowe J (2006) A bacterial dynamin-like protein. Nature 444:766-769.
1452 Low HH, Sachse C, Amos LA, Lowe J (2009) Structure of a bacterial dynamin-like protein lipid tube
1453 provides a mechanism for assembly and membrane curving. Cell 139:1342-1352.
1454 Nakhro KP, J.M. Choi, B.O. Chung, K.W. (2013) Missense mutations ofmitofusin 2in axonal
1455 CharcotMarieTooth neuropathy: polymorphic orincomplete penetration? Animal Cells and
1456 Systems Vol. 17: 228-236.
1457 Nicholson GA, Magdelaine C, Zhu D, Grew S, Ryan MM, Sturtz F, Vallat JM, Ouvrier RA (2008) Severe
1458 early-onset axonal neuropathy with homozygous and compound heterozygous MFN2
1459 mutations. Neurology 70:1678-1681.
1460 Notredame C, Higgins DG, Heringa J (2000) T-Coffee: A novel method for fast and accurate multiple
1461 sequence alignment. J Mol Biol 302:205-217.
1462 Ono T, Isobe K, Nakada K, Hayashi JI (2001) Human cells are protected from mitochondrial
1463 dysfunction by complementation of DNA products in fused mitochondria. Nature genetics
1464 28:272-275.
1465 Paradis E, Schliep K (2019) ape 5.0: an environment for modern phylogenetics and evolutionary
1466 analyses in R. Bioinformatics 35:526-528.
1467 Pipis M, Feely SME, Polke JM, Skorupinska M, Perez L, Shy RR, Laura M, Morrow JM, Moroni I,
1468 Pisciotta C, Taroni F, Vujovic D, Lloyd TE, Acsadi G, Yum SW, Lewis RA, Finkel RS, Herrmann

DN, Day JW, Li J, Saporta M, Sadjadi R, Walk D, Burns J, Muntoni F, Ramchandren S, Horvath R, Johnson NE, Zuchner S, Pareyson D, Scherer SS, Rossor AM, Shy ME, Reilly MM, Inherited Neuropathies Consortium - Rare Disease Clinical Research N (2020) Natural history of Charcot-Marie-Tooth disease type 2A: a large international multicentre study. Brain : a journal of neurology 143:3589-3602.

Piscosquito G, Saveri P, Magri S, Ciano C, Di Bella D, Milani M, Taroni F, Pareyson D (2015) Mutational mechanisms in MFN2-related neuropathy: compound heterozygosity for recessive and semidominant mutations. Journal of the peripheral nervous system : JPNS 20:380-386.

Poliacikova G, Barthez M, Rival T, Aouane A, Luis NM, Richard F, Daian F, Brouilly N, Schnorrer F, Maurel-Zaffran C, Graba Y, Saurin AJ (2023) M1BP is an essential transcriptional activator of oxidative metabolism during Drosophila development. Nat Commun 14:3187.

Rival T, Macchi M, Arnaune-Pelloquin L, Poidevin M, Maillet F, Richard F, Fatmi A, Belenguer P, Royet J (2011) Inner-membrane proteins PMI/TMEM11 regulate mitochondrial morphogenesis independently of the DRP1/MFN fission/fusion pathways. EMBO reports 12:223-230.

Rocha AG, Franco A, Krezel AM, Rumsey JM, Alberti JM, Knight WC, Biris N, Zacharioudakis E, Janetka JW, Baloh RH, Kitsis RN, Mochly-Rosen D, Townsend RR, Gavathiotis E, Dorn GW, 2nd (2018) MFN2 agonists reverse mitochondrial defects in preclinical models of Charcot-Marie-Tooth disease type 2A. Science 360:336-341.

Sali A, Blundell TL (1993) Comparative protein modelling by satisfaction of spatial restraints. J Mol Biol 234:779-815.

Sandoval H, Yao CK, Chen K, Jaiswal M, Donti T, Lin YQ, Bayat V, Xiong B, Zhang K, David G, Charng WL, Yamamoto S, Duraine L, Graham BH, Bellen HJ (2014) Mitochondrial fusion but not fission regulates larval growth and synaptic development through steroid hormone production. Elife 3.

Shahin S, Lu B, Zhou Y, Xu H, Chetsawang J, Baloh RH, Wang S (2023) MFN1 augmentation prevents retinal degeneration in a Charcot-Marie-Tooth type 2A mouse model. iScience 26:106270.

Silva Ramos E, Motori E, Bruser C, Kuhl I, Yeroslaviz A, Ruzzenente B, Kauppila JHK, Busch JD, Hultenby K, Habermann BH, Jakobs S, Larsson NG, Mourier A (2019) Mitochondrial fusion is required for regulation of mitochondrial DNA replication. PLoS genetics 15:e1008085.

Smith GA, Lin TH, Sheehan AE, Van der Goes van Naters W, Neukomm LJ, Graves HK, Bis-Brewer DM, Zuchner S, Freeman MR (2019) Glutathione S-Transferase Regulates Mitochondrial Populations in Axons through Increased Glutathione Oxidation. Neuron 103:52-65 e56.

Stavropoulos F, Sargiannidou I, Potamiti L, Kagiava A, Panayiotidis MI, Bae JH, Yeom SC, Lee JY, Kleopa KA (2021) Aberrant Mitochondrial Dynamics and Exacerbated Response to Neuroinflammation in a Novel Mouse Model of CMT2A. Int J Mol Sci 22.

Stuppia G, Rizzo F, Riboldi G, Del Bo R, Nizzardo M, Simone C, Comi GP, Bresolin N, Corti S (2015) MFN2-related neuropathies: Clinical features, molecular pathogenesis and therapeutic perspectives. Journal of the neurological sciences 356:7-18.

Tilokani L, Nagashima S, Paupe V, Prudent J (2018) Mitochondrial dynamics: overview of molecular mechanisms. Essays Biochem 62:341-360.

Tomaselli PJ, Rossor AM, Polke JM, Poh R, Blake J, Reilly MM (2016) Semi-dominant mutations in MFN2-related neuropathy and implications for genetic counselling. Journal of the peripheral nervous system : JPNS 21:52-54.

Twig G, Elorza A, Molina AJ, Mohamed H, Wikstrom JD, Walzer G, Stiles L, Haigh SE, Katz S, Las G, Alroy J, Wu M, Py BF, Yuan J, Deeney JT, Corkey BE, Shirihai OS (2008) Fission and selective fusion govern mitochondrial segregation and elimination by autophagy. The EMBO journal 27:433-446.

Verstreken P, Ly CV, Venken KJ, Koh TW, Zhou Y, Bellen HJ (2005) Synaptic mitochondria are critical for mobilization of reserve pool vesicles at Drosophila neuromuscular junctions. Neuron 47:365-378.

1519 Wakabayashi J, Zhang Z, Wakabayashi N, Tamura Y, Fukaya M, Kensler TW, Iijima M, Sesaki H (2009)
1520 The dynamin-related GTPase Drp1 is required for embryonic and brain development in mice.
1521 The Journal of cell biology 186:805-816.
1522 Wiederstein M, Sippl MJ (2007) ProSA-web: interactive web service for the recognition of errors in
1523 three-dimensional structures of proteins. Nucleic acids research 35:W407-410.
1524 Yan L, Qi Y, Huang X, Yu C, Lan L, Guo X, Rao Z, Hu J, Lou Z (2018) Structural basis for GTP hydrolysis
1525 and conformational change of MFN1 in mediating membrane fusion. Nature structural &
1526 molecular biology 25:233-243.
1527 Yun J, Puri R, Yang H, Lizzio MA, Wu C, Sheng ZH, Guo M (2014) MUL1 acts in parallel to the
1528 PINK1/parkin pathway in regulating mitofusin and compensates for loss of PINK1/parkin.
1529 Elife 3:e01958.
1530 Zhou Y, Carmona S, Muhammad A, Bell S, Landeros J, Vazquez M, Ho R, Franco A, Lu B, Dorn GW,
1531 2nd, Wang S, Lutz CM, Baloh RH (2019) Restoring mitofusin balance prevents axonal
1532 degeneration in a Charcot-Marie-Tooth type 2A model. J Clin Invest 129:1756-1771.
1533 Ziviani E, Tao RN, Whitworth AJ (2010) Drosophila parkin requires PINK1 for mitochondrial
1534 translocation and ubiquitinates mitofusin. Proceedings of the National Academy of Sciences
1535 of the United States of America 107:5018-5023.

1536